



Papers Presented at the

23 rd
annual

SUMMER INTERN CONFERENCE

August 9, 2007 — Houston, Texas

Papers Presented at the

**Twenty-Third Annual
Summer Intern Conference**

*August 9, 2007
Houston, Texas*

2007 Summer Intern Program for Undergraduates
Lunar and Planetary Institute

Sponsored by
Lunar and Planetary Institute
NASA Johnson Space Center

Compiled in 2007 by

Publications and Program Services Department
Lunar and Planetary Institute 3600 Bay Area Boulevard
Houston TX 77058-1113

Material in this volume may be copied without restraint for library, abstract service, education, or personal research purposes; however, republication of any paper or portion thereof requires the written permission of the authors as well as appropriate acknowledgement of this publication.

The Lunar and Planetary Institute is operated by the Universities Space Research Association and supported by the National Aeronautics and Space Administration under Cooperative Agreement No. NCC5-679 issued through the Solar System Exploration Division.

Any opinions, findings, and conclusions or recommendations expressed in this volume are those of the author(s) and do not necessarily reflect the views of the National Aeronautics and Space Administration.

AGENDA

- 8:00 a.m. Breakfast in LPI Great Room
- 8:30 a.m. Opening Statements by Dr. Julie Moses, Chair and Staff Scientist
- 8:40 a.m. **MICHAEL KAPLAN, Rice University** (Advisor: W. S. Kiefer)
Gravity Models of Large Impact Structures on Ancient Mars: Implications for Impact Processes and Crater Modification
- 9:00 a.m. **KELLYE ACUFF, Sul Ross State University** (Advisors: L. Danielson and K. Righter)
Partitioning of Phosphorus and Molybdenum in the Earth Mantle and the Conditions of Core Formation
- 9:20 a.m. **JOSEPHINE BOISSON, Institut de Physique du Globe de Paris**
(Advisors: E. Heggy and S. M. Clifford)
Exploring the Subsurface Ice-Enrichment in Athabasca Valles Using MARSIS Data
- 9:40 a.m. **JEREMY BROWN, Colorado School of Mines** (Advisor: Q. Li)
Volcano Topography and Apparent Viscosity of the Crust on Mars
- 10:00 a.m. **SYDNEY CHAMBERLIN, Utah State University** (Advisor: R. Christoffersen)
Computer Modeling of Solar Ion Radiation Processing of Planetary Surface Materials
- 10:20 a.m. Break
- 10:40 a.m. **LEAH CHEEK, College of William and Mary** (Advisor: D. A. Kring)
Cooling Rate Determination for H Chondrite Impact Melt Breccia LAP 02240
- 11:00 a.m. **JULIE COSMIDIS, Ecole Normale Superieure** (Advisors: E. Heggy and S. M. Clifford)
A Parametric Geoelectrical Model of the Martian North Polar Layered Deposits
- 11:20 a.m. **HANNAH ELKINTON, Mount Holyoke College** (Advisor: J. Jones)
Differentiation of the HED Parent Body
- 11:40 a.m. **ALEXIS HUMEAU, University of Bordeaux** (Advisors: E. Heggy and S. M. Clifford)
Parametric Electromagnetic Characterization of Ice-Dust Mixtures, to Support the MARSIS Data Analysis of the Martian Polar Layered Deposits (PLD)
- 12:00 p.m. **COLIN JACKSON, University of California, SC** (Advisors: J. Filiberto and A. Treiman)
Phase Stability Effects and Partitioning of Nickel Using the Humphrey Composition
- 12:20 p.m. Lunch
- 1:20 p.m. **EDGARD RIVERA-VALENTIN, Alfred University** (Advisors: M. R. Kirchoff and P. Schenk)
An Analysis of the Geologic Histories of Ganymede's Dark Terrain and Callisto Through Impact Cratering Distributions
- 1:40 p.m. **ANNELIESE LAWRENCE, Marshall University** (Advisors: J. F. Lindsay and S. K. Noble)
Forensic Analysis of Lunar Dust
- 2:00 p.m. **WILLIAM PITTMAN, University of Washington** (Advisor: T. F. Stepinski)
Building a Hydrological Database for Martian Valley Networks

- 2:20 p.m. **MARK SALVATORE, Pennsylvania State University** (Advisors: C. C. Allen and D. Z. Oehler)
The Geomorphic Evolution of Southwest Arabia Terra: Support for the 2009 Mars Science Laboratory Landing Site Selection Process
- 2:40 p.m. **JUSTIN TROYER, Purdue University** (Advisor: J. Moses)
Photochemical and Vertical Mixing Effects on the Atmospheric Chemistry of Gliese 229B
- 3:00 p.m. **Adjourn — Group Photo**

CONTENTS

Partitioning of Phosphorus and Molybdenum in the Earth Mantle and the Conditions of Core Formation <i>K. M. Acuff, L. Danielson, and K. Righter</i>	1
Exploring the Subsurface Ice-Enrichment in Athabasca Valles Using MARSIS Data <i>J. Boisson, E. Heggy, S. M. Clifford, and A. Frigeri</i>	4
Volcano Topography and Apparent Viscosity of the Crust on Mars <i>J. Brown and Q. Li</i>	7
Computer Modeling of Solar Ion Radiation Processing of Planetary Surface Materials <i>S. J. Chamberlin and R. Christoffersen</i>	10
Cooling Rate Determination for H Chondrite Impact Melt Breccia LAP 02240 <i>L. C. Cheek and D. A. Kring</i>	13
A Parametric Geoelectrical Model of the Martian North Polar Layered Deposits <i>J. Cosmidis, E. Heggy, S. M. Clifford, and A. Humeau</i>	16
Differentiation of the HED Parent Body <i>H. Elkinton and J. Jones</i>	19
Parametric Electromagnetic Characterization of Ice-Dust Mixtures, to Support the MARSIS Data Analysis of the Martian Polar Layered Deposits (PLD) <i>A. Humeau, E. Heggy, S. M. Clifford, and J.-L. Miane</i>	22
Phase Stability Effects and Partitioning of Nickel Using the Humphrey Composition <i>C. Jackson, J. Filiberto, A. Treiman, and L. Le</i>	25
Gravity Models of Large Impact Structures on Ancient Mars: Implications for Impact Processes and Crater Modification <i>M. S. Kaplan and W. S. Kiefer</i>	28
Forensic Analysis of Lunar Dust <i>J. A. Lawrence, J. F. Lindsay, and S. K. Noble</i>	31
Building a Hydrological Database for Martian Valley Networks <i>W. Pittman and T. F. Stepinski</i>	34
An Analysis of the Geologic Histories of Ganymede's Dark Terrain and Callisto Through Impact Cratering Distributions <i>E. G. Rivera-Valentin, M. R. Kirchoff, and P. Schenk</i>	37
The Geomorphic Evolution of Southwest Arabia Terra: Support for the 2009 Mars Science Laboratory Landing Site Selection Process <i>M. R. Salvatore, C. C. Allen, and D. Z. Oehler</i>	40
Photochemical and Vertical Mixing Effects on the Atmospheric Chemistry of Gliese 229B <i>J. Troyer and J. Moses</i>	43

Partitioning of phosphorus and molybdenum in the Earth mantle and the conditions of core formation

K.M. Acuff¹, L. Danielson², K. Righter², ¹Lunar and Planetary Institute Houston, TX ²Johnson Space Center Houston, TX

Introduction: Something that seems to puzzle the minds of many planetary scientists is the understanding of how the terrestrial planets formed and differentiated. There are several hypotheses on the specific processes that might have occurred during the formation of the Earth. One hypothesis that has been proposed is that early in the Earth's formation, there was a magma ocean present, (Li and Agee, 1996), and within this body, siderophile elements separated out of the silicate liquid to form the metal core (Righter, 2003). This study addresses this hypothesis.

P and Mo are moderately siderophile elements that are present in both the mantle and the core (Agee and Martin, 2007). The concentrations of P and Mo in silicate vs. metal can be measured and in turn used to determine the temperatures, pressures, oxygen fugacity and melt composition required to achieve the same concentrations as observed in the mantle.

The data here include eight experiments examining the partitioning of P and Mo between metallic liquid and silicate liquid. The purpose of the experiments has been to gain a greater understanding of core-mantle separation during the Earth formation process and examines temperature effects on P and Mo, which has not been systematically studied before.

Procedures: The sample used in this series of experiments was composed of 70% Knippa Basalt, the composition of which is described in Lewis et al. (1993), 29% Fe and 1% MoO₃. These were ground to a powder and mixed. Two types of capsules were used: graphite and MgO. Most runs were conducted at a constant pressure using a piston cylinder apparatus. Once the samples were under pressure, they were heated to silicate superliquidus temperatures and allowed to equilibrate for a set amount of time depending on the run temperature. A Type C thermocouple (W-Re) wire with an accuracy of $\pm 2^\circ$ C was used to measure the temperature. The samples were then quenched to a silicate glass containing large metallic liquid spheres (Fig. 1). Quenching occurred by turning off the power.

The two different temperature series consisted of eight successful runs at 10.3 kbars and at temperatures between 1500° and 1800° C (Table 1). Run durations were chosen based on equilibration times from previous experiments (Righter et al., 1997, Li and Agee, 1996).

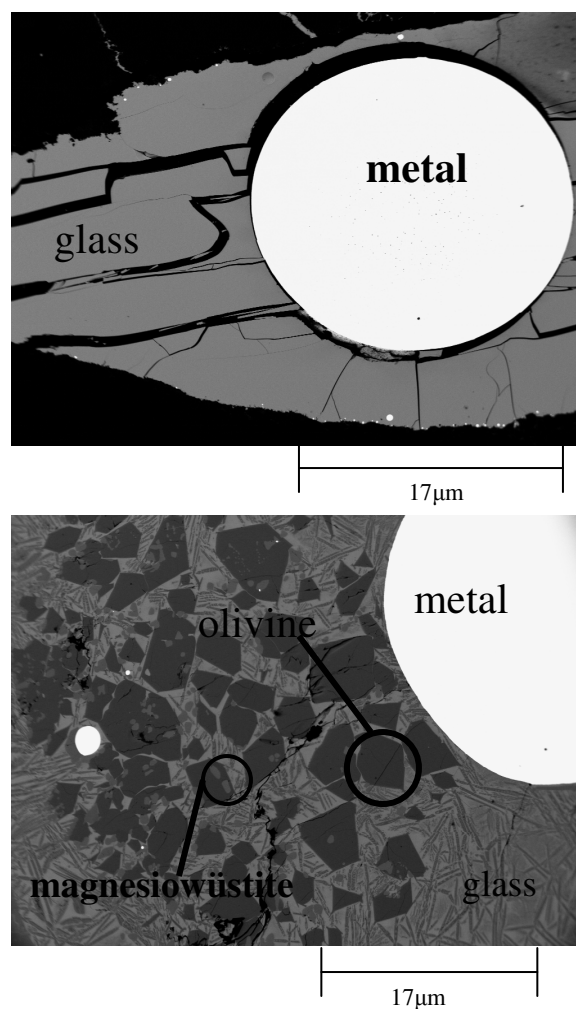


Fig. 1. cow25 (top) showing graphite capsule (black), silicate glass (grey) and metal blobs (white); cow12 (bottom) showing silicate glass with dark olivine and light magnesiowüstite crystals (grey) and metal blobs (white).

Analysis: Samples were analyzed for major element composition using the electron microprobe at NASA-JSC including Mo concentrations in the metal. The operating conditions included an accelerating voltage of 20 kV and sample current of 20 nA (Righter et al., 2006). The standards used were GaP, Mo metal, Fe metal, CaSiO₃, kaersutite, hematite, rhodonite, albite, and potassium feldspar. Samples cow1, cow3, cow8 and cow20 were run using the graphite capsules, causing the metal spheres to be C saturated. Wt% C

Table1. Summary table of all experiments in this study

Sample	Temperature	Pressure	Duration	$\Delta\log f_{O_2}$	Capsule	D_P
cow1	1500° C	10.3 kbars	3 hrs	-1.437	graphite	0.336
cow3	1600° C	10.3 kbars	90 min	-1.475	graphite	0.399
cow8	1700° C	10.3 kbars	45 min	-1.447	graphite	0.309
cow20	1800° C	10.3 kbars	15 min	-1.435	graphite	0.690
cow10	1500° C	10.3 kbars	3 hrs	-1.596	MgO	0.070
cow12	1600° C	10.3 kbars	90 min	-1.762	MgO	0.407
cow17	1700° C	10.3 kbars	45 min	-1.764	MgO	0.004
cow16	1800° C	10.3 kbars	15 min	-1.813	MgO	0.161

was calculated based on the melting temperature of each run using the Fe-C phase diagram showing graphite solubility in liquid phase (Sundman et al., 1985). The calculated amounts were 4.50 wt% in cow1, 4.7 wt% in cow3, 4.9 wt% in cow10 and 5.5 wt% in cow20.

Mo in the silicate at ppm levels was analyzed using the Laser Ablation- Inductively Coupled Plasma- Mass Spectrometer (LA-ICP-MS) at Rice University. The LA-ICP-MS uses a laser beam to ablate the sample allowing the elements within a certain area to be converted to plasma which is sent into the mass spectrometer. A magnet is tuned to allow Mo, as well as many other isotopes, to be counted. The standards for this analysis were NIST610 and 612 glasses, BCR and BHVO glasses, and Hoba iron meteorite. The data collected from these analyses was not prepared in

time for this particular summary and any results discussed further will consist of mostly P data.

Results: Wt% P and Mo were measured in the metal and silicate of each sample. In the metal spheres, P was measured at ~0.02 to 0.60 wt% and Mo was measured at ~0.70 to 3.20 wt%. In the silicate glasses, P was measured at ~0.10 to 0.35 wt%. These values were consistent throughout all eight experiments.

There were measurable variations in wt% MgO with increasing temperature for the four experiments that were run in MgO capsules (Fig. 2). The sample originally contained ~13% MgO but as the basalt reacted with the capsules, the amount of MgO within the sample increased to >13% (Fig 4). The 1600° run (cow12) did not show the dramatic increase in MgO like the other three runs. During quenching of the cow10 and cow12 runs, olivine and/or magnesiowüstite crystals formed within the silicate (Fig. 1). These were analyzed and the olivine crystals showed to have an average of 49.83 to 53.20 wt% MgO however the magnesiowüstite crystals had an average of 77.99 wt% MgO (Table 2). This crystal formation resulted in the MgO being removed from the silicate in the cow12 run.

It is important to understand the varying natures of P and Mo. Because Mo is a refractory element, any evidence of depletion that may occur in Mo concentrations in Earth's mantle is due to core formation and so can be directly interpreted as such whereas depletion in P concentrations may be due to the volatility of the element as well as core formation. This creates some difficulty in interpreting data that is collected on wt% P in the melts.

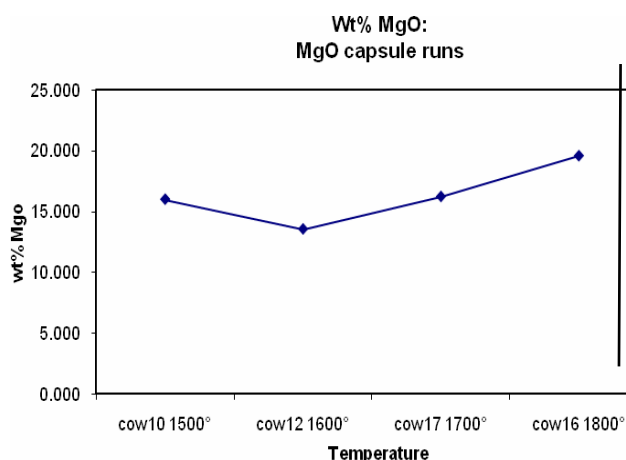


Fig.2 Concentrations of MgO in the four experiments that were run in MgO capsules: cow10, cow12, cow17 and cow16.

Table 2. Average compositions of olivine and magnesia-wustite crystals in silicate quench of cow10 and cow12.

Sample	SiO ₂	FeO	MgO	MnO	Total
Cow10 olivine	41.02	8.92	49.83	0.19	99.96
Cow12 olivine	41.69	4.90	53.20	0.08	100.14
Cow12 Mg-wustite	0.04	20.60	77.99	0.13	98.76

Oxygen fugacity (f_{O_2}) is also necessary to take into consideration because the partition coefficients will change along with it. The f_{O_2} for the samples was calculated for this study (Table 1) as a logarithmic function of the ratio of Fe in the metal and FeO in the silicate.

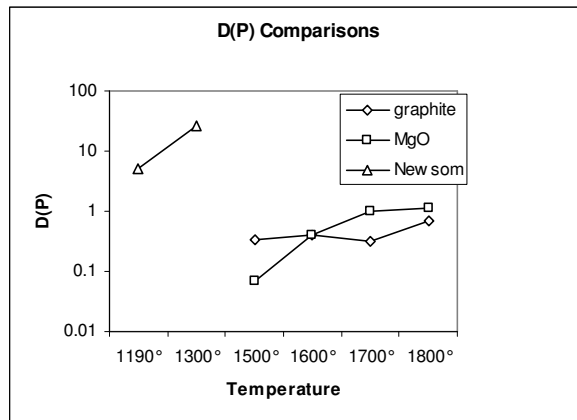


Fig. 3 Plot showing a comparison of D_P from three data sets. The three series include experiments run in graphite capsules, experiments run in MgO capsules and the two data points from a study by Newsom and Drake (1982).

Figure 3 shows the results from the eight experimental runs that were analyzed for this project along with the 1190° and 1300° C data from a study done by Newsom and Drake (1982). There were two data sets from this study and one data set from the Newsom and Drake study. These three sets of data were compared and showed a similar trend that agrees with the idea that increasing temperature will in fact increase D values for P. The four experiments that were run with graphite capsules did not seem to show as much of a change in D values from 1500° to 1800° C as the experiments that were run in the MgO capsules did.

Discussion: The information in this study can be applied to the current understanding about the

conditions necessary to achieve the current concentrations of P in the mantle. A D_P value of 30 (Righter et al., 1996) is required to explain the mantle P concentrations, and this value is much greater than any achieved with the experiments in this study. Based on the data here, and in other studies predicting an increasing D value for P with increasing temperature (Righter and Drake, 1999), it is assumed that higher temperatures are needed to reproduce current mantle concentrations of P. Further research that will include high pressure and temperature experiments using an 880-ton multi anvil press might be able to better achieve these conditions. With information from further experimentation as well as Mo data collected from the LA-ICP-MS, perhaps these questions can be answered.

References:

- Agee C.B. et al, 2007 Molybdenum solubility in silicate melt at high pressures and temperatures: experimental constraints on planetary core formation. *LPS XXXVII*, abstract # 2170.
- Lewis R.D. et al. 1993 The effect of Na vapor on the Na content of chondrules. *Meteorites* 28: 622-628.
- Li J. and Agee C.B. 1996 Geochemistry of mantle-core formation at high pressure. *Nature* 381: 686-689.
- Newsom H.E. and Drake M.J. 1982 Experimental investigation of the partitioning of phosphorus between metal and silicate phases: implications for Earth, Moon and Eucrite Parent Body. *Geochemica et Cosmochemica* 47: 93-100.
- Righter K. 2003 Metal-Silicate Partitioning of siderophile Elements and Core Formation in The early Earth, *Annu. Rev. Earth Planet Sci.* 31:135-74
- Righter K. and Drake M. 1999 Effects of water on metal-silicate partitioning of siderophile elements: a high pressure and temperature terrestrial magma ocean and core formation. *Earth and Planetary Science Letters* 171: 383-399.
- Righter K., et al. 2006 An experimental study of the oxidation state of vanadium in spinel and basaltic melt with implications for the origin of planetary basalt. *American Mineralogist* 91: 1643-1656.
- Righter K., et al. 1996 Prediction of siderophile element metal-silicate partition coefficients to 20 GPa and 2800° C: the effects of pressure, temperature, oxygen fugacity, and silicate and metallic melt compositions. *Physics of the Earth and Planetary Interiors* 100: 115-134.
- Sundman B. et al. 1985 A thermodynamic assessment of the Fe-C system. *Calphad* 9: 153-190.

Exploring the Subsurface Ice-Enrichment in Athabasca Valles Using MARSIS

Data: Boisson J.¹, E.Heggy², S.M. Clifford², A.Frigeri³, ¹Institut de Physique du Globe de Paris, Paris, France (boisson@ipgp.jussieu.fr), ²Lunar and Planetary Institute, 3600 Bay Area Blvd, Houston, TX 77058-1113, USA, ³University of Perugia, Perugia, Italy

Introduction: Thermal models of the Martian subsurface suggest the potential presence of a global aquifer at depths ranging from an estimated average depth of 3 km at the equator to 8 km in the polar regions. This aquifer would be protected from sublimation by a region of frozen ground known as the cryosphere [1,2]. Geomorphologic observations of the Martian surface support the hypothesis that a substantial amount of water may reside in the subsurface [3].

In order to constrain the ambiguities regarding the presence of subsurface water, two low-frequency sounding radars, MARSIS (Mars Advanced Radar for Subsurface and Ionosphere Sounding) and SHARAD (SHallow subsurface sounding RADar) are probing the upper crust in an attempt to map, localize and identify potential hydrogeological features that can trace the origin and evolution of the Martian hydrosphere.

In this effort, we explore the dielectric properties of the Martian subsurface in the equatorial area of Athabasca Vallis as a key area in constraining the presence of ice in the subsurface. In our approach, we compare the MARSIS radar backscattered echoes over this area to those generated by Finite Difference Time Domain (FDTD) radar simulations based on several plausible geoelectrical scenarios of the subsurface.

Geological Context of Athabasca Vallis: Athabasca Vallis is located at approximately 5°N and 150°E, in the vicinity of Cerberus Fossae. This tectonic fissure is the source of the late Amazonian (2-10 My) lava flows that are observed in this area [4]. Recently, HRSC discovered broken, rafted-plate morphology (Fig. 1) that can be explained by two formation hypothesis:

(1) The first hypothesis is a hydrologic one, where the observed geomorphology in Athabasca Vallis is mainly shaped by mechanisms that involve the discharge of large quantities of ground water onto the surface. This liquid water would have frozen gradually by forming pack-ice on the surface. Volcanic ash may have then covered these features, hence protecting the pack-ice from sublimation [4].

(2) The second hypothesis is based on a volcanic event. A large amount of extruded low viscosity lava may have formed a lava lake. On the surface, the crystallization of the magma resulted in the formation of solidified crust. This crust would have then been fractured and moved by the flow of the still-liquid lava underneath. Finally, as the whole lava lake cooled and solidified, it would have preserved the broken, rafted plate morphology on the surface.

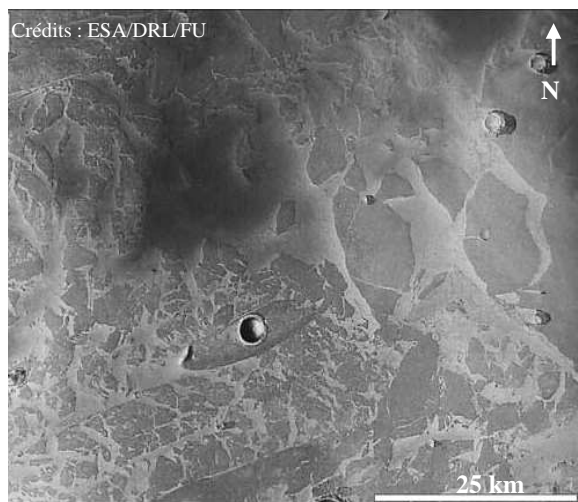


Figure 1. HRSC image centered at 5.5°N latitude and 150.4° E longitude, in the area of Athabasca Vallis. We can see break-up plate features [4]

Geoelectrical Context: In order to quantitatively interpret the MARSIS radar echoes over Athabasca Vallis, a minimum knowledge of the subsurface geoelectrical properties is required. Hence, we constructed different geoelectrical models of the shallow subsurface. Those models are the used as the basis for the FDTD radar backscattered simulations. The geoelectrical models are elaborated and constrained from the current state of knowledge of the Athabasca area as observed by TES, HRSC and THEMIS. The geoelectrical model is shown in Table 1.

The TES data of the central peak of a large impact crater in the northern of Athabasca Vallis (9°N, 150°E) indicate that the bedrock is composed of andesitic material [6]. This would suggest that

the deep subsurface layers are mainly constituted of andesitic material (likely interbedded with pyroclastic material). In order to investigate the two formation hypothesis of Athabasca Vallis (hydrologic and volcanic), both our models assume an ice layer contaminated with different amounts of basaltic dust (Table 1). The ice layer of the first model (the hydrologic hypothesis) is contaminated by 20% of basaltic dust. The second model (the volcanic hypothesis) is represented by an ice layer with 80% basaltic dust contamination. Finally, the two models are covered by a layer of volcanic ash (reducing sublimation), and eolian dust.

The dielectric properties (at 2 MHz) of these four layers are indicated in Table 1. They are derived from lab measurements of analog materials [7,8]

Radar Echo Simulation: To constrain the penetration depth of MARSIS signal in the shallow subsurface of Athabasca Vallis, we used the FDTD technique [9] that solves the Maxwell's equations in discrete steps of time and space, making it possible to study radar wave propagation across parametrical geoelectrical models [10].

The depth of the simulation space is 150 m. Its width is $500 \text{ m} \times 500 \text{ m}$, in order to reduce multiple scattering from the assumed geometry's sharp edges. This simulation space is divided into elementary cells of $2 \times 2 \times 2 \text{ m}$. The emitted signal is a plane wave (polarized in Ex) with maximum amplitude of 1 V/m. The emitted waveform is a modulated Gaussian with a central frequency of 1-5 MHz.

Simulation results yield the magnitude of the backscattered electric field as function of the wave propagation time. In order to compare this result with MARSIS radar data at 5 MHz, we applied to the simulation output an inverse Fourier transform that allowed us to simulate the same frequency

band as MARSIS. Then, we calculated the signal losses in dB (Fig.2) for the propagation time. We observed that the ice layer contaminated with 80% of basaltic dust generates stronger losses than the first model having 20% of dust (2 to 5 dB of differences between the two models).

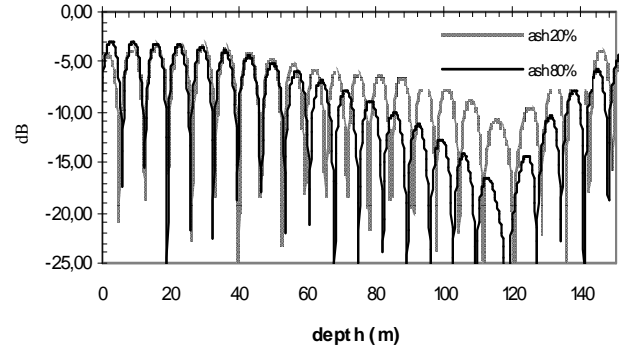


Figure 2. simulation at 1-5 MHz of the backscattered radar signal losses as function of the depth. Dashed line : 20% of ash – Black line : 80% of ash

MARSIS Data Analysis: MARSIS radar data presented here are from the 5 MHz-band of the Mars Express orbit 4092. The profile is composed of 119 traces (magnitude in V/m) along a track from 0° to 10° north latitude and centered on 149.2° east longitude.

We applied a temporal filter to the data in order to eliminate background noises. Similarly to the simulated echoes, we calculated the signal losses in dB. The Figure 3 shows the MARSIS radargram (in normalized dB) with the topographic profile of Athabasca Vallis area from MOLA data.

Finally, we compared radar traces of the northern part of the radar profile with the traces of the southern part in order to explore the potential presence of lithologic variations along this north-south profile. To perform this, we stacked 14 traces

Table 1. Dielectric properties (2 MHz) of the different geological layers [7,8].

Geological material	ϵ'	ϵ''	σ (S/m)	thickness(m)
Dust	3.40	0.080	$8.897 \cdot 10^{-6}$	5
Volcanic ash	5.50	0.120	$1.335 \cdot 10^{-6}$	15
Ice layer with 20% of basaltic dust (model 1)	3.15	0.0057	$6.306 \cdot 10^{-7}$	40
Ice layer with 80% of basaltic dust (model 2)	4.50	0.022	$2.402 \cdot 10^{-6}$	
Lava flows	8.00	0.320	$3.559 \cdot 10^{-5}$	90
Pyroclastic deposit	6.00	0.084	$9.349 \cdot 10^{-6}$	

data from 5° to 6.18°N and from 8.8 to 9.97°N to increase the noise to signal ratio level (Fig.4).

Figure 4 also shows that, in the south of the profile, the exponential losses (characteristic of relatively homogenous layer) are 16 dB in the first 300 meters while they are only of 12 dB in the north.

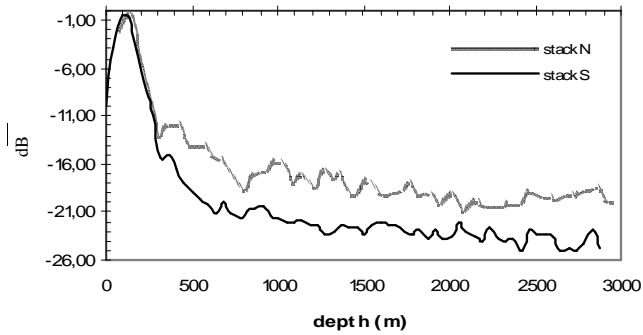


Figure 4. Comparison of the radar signal losses (stack of 14 tracks) between the northern part and the southern part of the radar profile in the area of Athabasca Vallis.

Discussion and Conclusion: The radar signal losses generated by the different geologic layers in the center of Athabasca Vallis (around 5.5°N) are stronger than those observed on the north of the profile. In the first 300 meters, the radar signal loses 0,053 dB/m in the south of the profile. In the north, the radar signal loses only 0,04 dB/m.

The results of the radar echo simulation show that a lithologic variation in the shallow subsurface

can generate important signal losses variations (even if the depth sounding is shorter than the signal wavelength). The observed difference of losses along the MARSIS radar profile can thus be explained by a lithologic variation of the shallow subsurface, the radar signal recording more losses in the south than in the north of the profile.

Although we cannot exclude it, the presence of a pure-ice-rich layer in the subsurface of Athabasca Vallis does not appear to explain the preliminary result obtained from the losses analysis of the MARSIS data.

Further works will be based on more MARSIS and SHARAD data analysis to conclude on the formation of the pack-ice-like morphology in the area of Athabasca Vallis. The results presented here will have to be supplemented by SHARAD, OMEGA (spectrometer on board Mars Express) and HRSC data.

References: [1] Clifford S.M. (1993) *JGR*, 98, 10,973-11,016. [2] Clifford S.M. and Parker T.J. (2001) *Icarus*, 154(1), 40-79. [3] Malin M.C. and Edgett K.S. (2000) *Science*, 288, 2330-2335. [4] Murray J.B. et al. (2005) *Nature*, 434, 352-355. [5] Keszthelyi L. et al. (2000) *JGR*, 105, E6, 15,027-15,049. [6] Christensen P.R. et al. (2001) *JGR*, 106, 23,823-23,871. [7] Heggy E. et al. (2006) *JGR*, 111, 1-16. [8] Grimm R.E. (2006) *JGR*, 111, E06, 2619-2634. [9] Yee K.S. (1966) *IEEE Trans Antennas propagation*, 14, 3,302-3,307. [10] Heggy E. et al. (2003) *JGR*, 108, E4, 11,1-11,10.

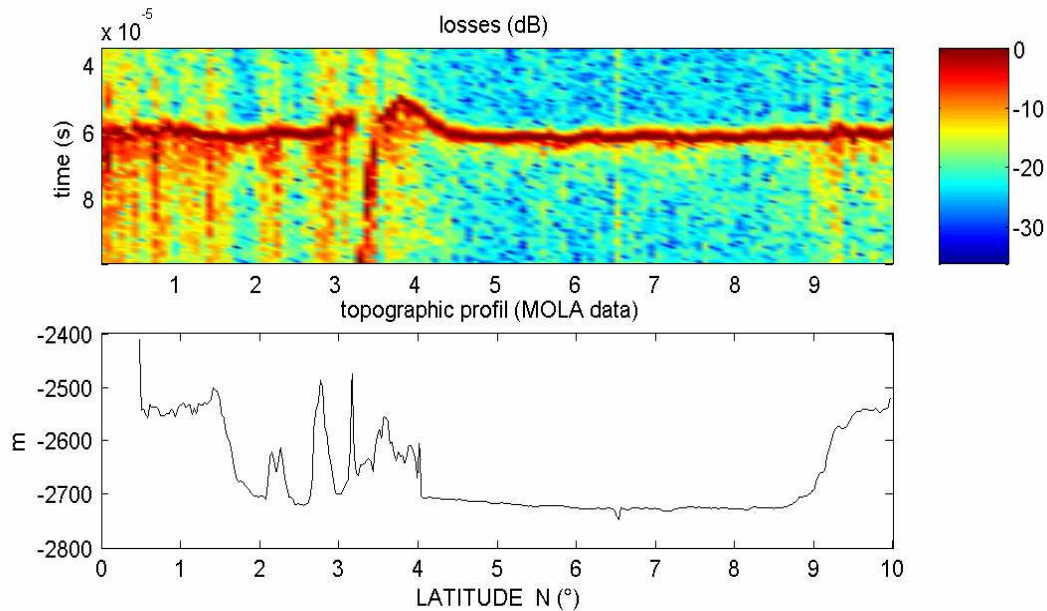


Figure 3. Top: losses radargram (in dB) from MARSIS data orbit 4092 (band 5MHz) between 0° and 10° north latitude - Bottom: topographic profile of Athabasca Vallis from MOLA data.

Volcano Topography and Apparent Viscosity of the Crust on Mars. Jeremy Brown¹, Qingsong Li²; ¹Department of Geophysics, Colorado School of Mines, Golden, CO 80401 (email: jerbrown@mines.edu); ²Lunar and Planetary Institute, 3600 Bay Area Boulevard, Houston, TX 77058

Introduction

The lithosphere of Mars experiences little deformation and forms a single plate. However, observational evidence, including extensional grabens and slope change of crustal dichotomy, indicate non-zero crustal deformation [1, 2]. It is highly likely that volcanoes, the largest topographic features on Mars, experience substantial crustal deformation. This research project seeks to explore the potential viscous deformation of the crust on Mars and put constraints on the average apparent crustal viscosity by focusing on the Martian volcano topography and its change through time.

The major hypotheses related to the volcano topography on Mars include: 1) there is no significant or detectable deformation occurring on the volcanoes of Mars because the topographic differences among the volcanoes are due to their varying lava compositions; 2) there has been continuous viscous relaxation of the crust, regardless of volcano composition, beginning with the formation of the volcanoes. The research presented in this paper focuses on the scenario of continuous viscous relaxation of the crust.

In many previous Martian lithosphere dynamic studies, the lithosphere, including the crust, is assumed to be elastic or elastic-frictional [3]. Viscous deformation on Mars has been considered in a few studies, but mostly in relation to the crustal dichotomy of Mars and for several giant basins. The changes in crustal thickness and lower crustal flow between the southern highlands and northern lowlands have been considered, but whether there is significant viscous deformation is under debate [2, 4]. This may be because the deviatoric stress in these regions is low (lower than the stress underneath the volcanoes) and the crustal viscosity is high.

With volcanoes, which are high topographic features, there is a greater gravitational load on the crust and lithosphere and considerably higher deviatoric stress. According to a stress-dependent viscosity law, higher stress may cause lower apparent viscosity. Consequently, with a higher stress and lower viscosity, it will be easier to detect viscous deformation on volcanoes than other regions such as the crustal dichotomy or impact basins.

Modeling

Using a digital elevation program, GRIDVIEW, the present-day topographic profiles of fifteen major volcanoes on Mars are estimated. The profiles are plotted against each other for each volcano. The average slope for each volcano is determined enabling us, with estimated volcano widths, to calculate the initial height for each of the volcanoes. These initial heights are used for viscous deformation simulation purposes and are different from the actual volcano height, which is characterized with a low elevation caldera.

In order to study exactly how a particular volcano will deform under certain parameters, a semi-analytical viscous flow model, assuming uniform linear viscosity in the crust, is used to investigate how deformation changes according to changes in the width, height, crustal thickness, and viscosity. A reference volcano is used in order for the changes and effects to be seen when parameters were varied. In addition to exploring the effects of volcano parameters, we also want to observe under what conditions the volcanoes of Mars deform. To accomplish this task, bounds are set on the viscosity. Preliminary constraints are placed on the crustal viscosity by assuming either no detectable viscous deformation or significant viscous flattening from initial volcano topography. To determine the viscous evolution of crustal thickness, we use its corresponding rate of change formula,

$$\frac{\partial D}{\partial t} = \frac{\Delta \rho g}{12\eta} \frac{\partial(r \frac{\partial D}{\partial r} D^3)}{r \partial r},$$

where D is the crustal thickness, g is the gravitational acceleration, η is the viscosity of the crust, $\Delta \rho$ is the density difference between the crust and mantle, and r is the radius from the volcano center. Airy's isostasy is assumed.

The lithosphere appears to be elastic in short-term and viscous in long-term. In the time-scale of Mars' history, both elastic and viscous properties may affect volcano deformation. On early Mars, the lithosphere was thin. As the planet cooled the lithosphere became thicker [3, 5]. Consequently, the lithosphere is able to support more and, hence, we see an elastic effect. The initial semi-analytical viscous flow model solely incorporated viscous relaxation and ignores any elastic effects. In order to fully investigate and understand the viscosity of the lithosphere, another numerical model is used that assumes, in addition to a linear viscous behavior, a linear elastic behavior. The model assumes a Maxwell visco-elastic rheology in which

$$\dot{\epsilon} = \frac{\dot{\sigma}}{\kappa} + \frac{\sigma}{\eta},$$

where $\dot{\epsilon}$ is the strain rate, κ is rigidity of the crust, σ is stress, and $\dot{\sigma}$ is the stress rate. The model uses the finite element method in order to solve for the edifice topographic displacement over time. Airy's isostasy is assumed for the initial volcano configuration while it becomes a dynamic approximation over time [6]. Through this model we gain a better understanding of the complete rheology that considers both viscosity and elasticity.

Results

Depending on the changes in particular parameters, the effects on viscous deformation of a volcano vary. Through several different semi-analytical simulations, a better idea of the effects due to the changes in volcano width, crustal thickness, and viscosity can be drawn. All the simulations show volcano deformation over a two billion year period. With an increase in the width of a volcano, there is a lower rate of deformation within the given time period. Consequently, a greater width decreases the rate of deformation through time. The effects of changes of viscosity, one of the most important concepts related to this project, can be described in a general sense. As viscosity increases in the crust, there is a lower rate of deformation. The lower the viscosity, the higher rate of deformation takes place. If the viscosity is too high, then deformation cannot be measured or detected. Crustal thickness, important to lower crustal flow and viscous relaxation, plays a vital role in relaxation over time. An increase in crustal thickness yields a higher rate of deformation as a decrease yields a lower rate.

Using the semi-analytical viscous flow model, lower and upper bound constraints were placed on the viscosity of the crust. An upper bound is placed in order to determine the point in which deformation is undetectable. If the viscosity is above the upper bound, then there is no significant or detectable deformation occurring. On the other hand, if the viscosity is smaller than the upper bound, then there is greater than ten percent deformation (height change over initial height) occurring within a two billion year period. A lower bound is set to determine the point in which the volcano deforms from an initial shape to the present-day shape within two billion years. The initial shape here is assumed to have a slope equal to the largest volcano slope at present-day (Tharis Tholus). The average upper bound viscosity is around 1×10^{27} Pa s (50000m crustal thickness)(Fig. 1) whereas the average lower bound viscosity is around 1×10^{25} Pa s (50000m crustal thickness)(Fig. 2). Assuming a 100000m crustal thickness, the average upper bound viscosity is in the 1×10^{27} to 1×10^{28} Pa s range and the average lower bound viscosity is in the 1×10^{25} to 1×10^{26} Pa s range.

The visco-elastic numerical model, incorporating viscous and elastic effects, presents evidence for a strong elastic effect with respect to volcano deformation. When only viscous relaxation is considered, there is greater deformation at the volcano summit and at the foot of the volcano. Since these parts of the volcanoes do not deform as much and the volcano slope changes more when an elastic effect is added, we can see that an elastic effect is influential over the overall relaxation and subsidence of each volcano (Fig. 3).

The visco-elastic numerical model is applied assuming significant flattening from initial volcano topography, which is assumed to have the same slope as Tharsis Tholus. We are able to set a lower bound on the viscosity at 1×10^{25} to 1×10^{26} Pa s through simulations on several volcanoes. This viscosity bound is close to the set with the solely viscous semi-analytical model.

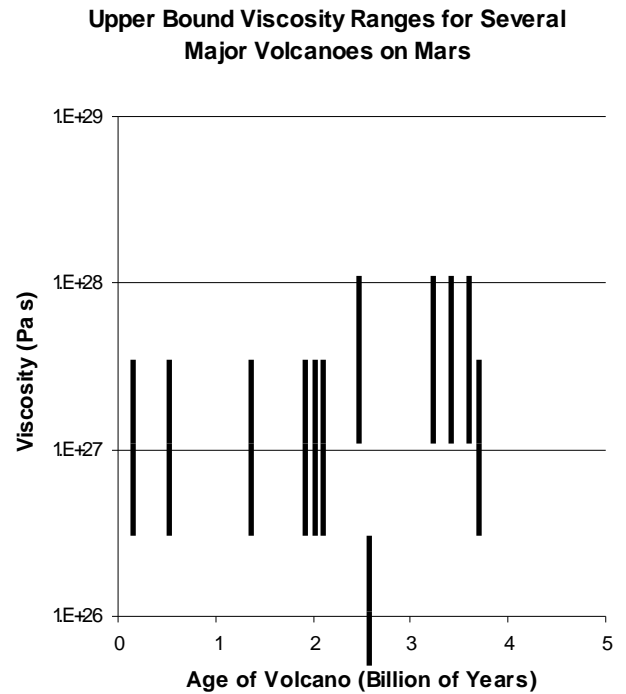


Figure 1: The upper bound viscosity constraints for several major volcanoes on Mars assuming a 50000m crustal thickness.

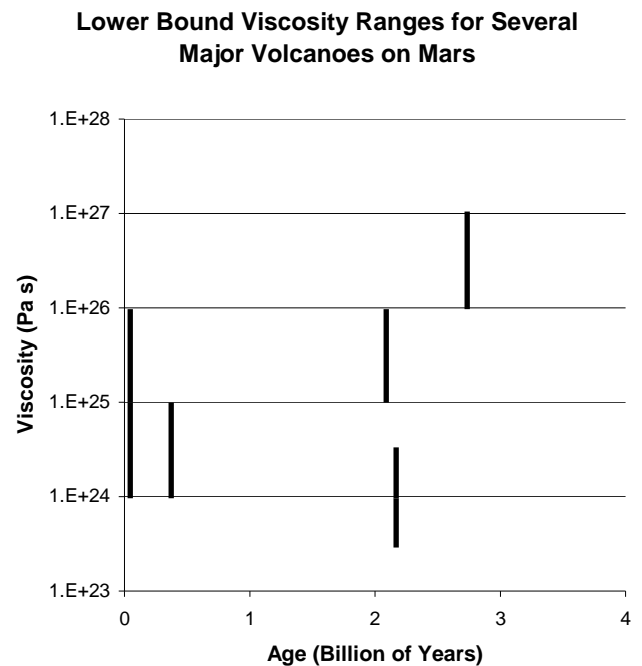


Figure 2: The lower bound viscosity constraints for several major volcanoes on Mars assuming a 50000m crustal thickness.

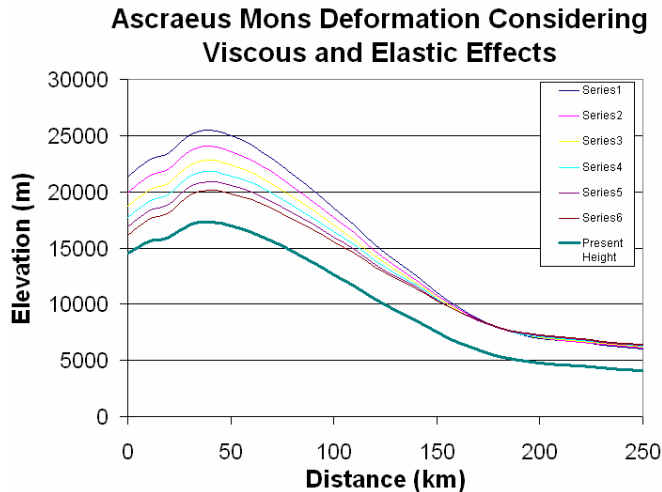


Figure 3: Volcano deformation simulation of Ascreaeus Mons showing relaxation from initial volcano topography over 3 billion years. Crustal thickness equals 5×10^{25} Pa s.

Discussion

Previous lithosphere deformation studies have used viscous relaxation to determine crustal thickness [4]. The crustal composition has also been used to determine the extent of viscous relaxation by setting parameters based on the amount of water and how such water influences the strength of the crust and/or mantle [2]. With these studies come many uncertainties and many assumptions in crustal composition, mineral rheology, and the thermal field of the lithosphere. In this project, we seek to use a simple model in order to give a crustal viscosity range by avoiding the compositional, thermal and experimental uncertainties.

The results yield no consistent correlation between the viscosity of a particular volcano and the volcano's age. Although this is the case, it is hard to determine the exact formation age of the volcanoes on Mars. The estimated ages are surface ages and not the true formation ages [7, 8]. The surface age is probably considerably younger than the formation age due to the fact that substantial volcanism occurs in early Martian history and decays rapidly through time. There could potentially be a relationship, but not with volcano surface ages.

For the Earth, several different methods are used to determine lower crustal viscosity. One method is post-seismic relaxation. After an earthquake, the deformed crust generates viscous relaxation. This relaxation can be measured to calculate lower crustal viscosity. Post-glacier is also a useful method on Earth to measure the lower crust and upper mantle viscosity. By measuring the speed of the rebound, we can calculate the viscosity. Additional methods include using

experimental data to measure the viscosity of rocks and minerals to gain a better understanding of the rheology of the crust. Unfortunately, we do not have the means to perform such methods on Mars yet. Unlike the Earth, though, where the viscosity can be measured back to just a few tens of thousands of years, we can measure the viscosity of Mars up to several billion years. It has been suggested that the apparent viscosity may significantly vary with the time-scales of loading history. This project is unique because it has afforded us the opportunity to determine the long-term viscosity, up to three billion years, of the crust on Mars. Conducting simulations on several different volcanoes of varying size, shape, and age and finding their viscosities to be within one order of magnitude from one another, reveal that the viscosity of the crust does not vary significantly and does not necessarily depend on the characteristics of a volcano.

Conclusion

With Martian volcano topography, constraints are placed on the viscosity of the crust using a simple semi-analytical viscous model and a numerical visco-elastic model. The upper viscosity bound for significant viscous deformation is $1 \times 10^{27} - 1 \times 10^{28}$ Pa s. The lower viscosity bound to sustain each volcano to the present-day shape is $1 \times 10^{25} - 1 \times 10^{26}$ Pa s. The pattern of visco-elastic volcano deformation is different from that of solely viscous deformation. The solely viscous model predicts more deformation at the summit and foot of the volcanoes while the visco-elastic model predicts more deformation of the volcano slope change. Unlike the Earth, the long history of Martian volcanoes gives us a unique opportunity to estimate the long-term crustal viscosity in the time scale of billions of years.

Acknowledgements

I would like to thank my advisor, Dr. Qingsong Li, for his support, help, and guidance during the internship program and the Lunar and Planetary Institute for giving me an opportunity to take part in this excellent research experience.

References

- [1] P.J. McGovern *et al.* (2001) *JGR*, 106, 23769-23809. [2] A. Guest and S. E. Smrekar (2007) *Physics of the Earth and Planetary Interiors*, doi:10.1016/j.pepi.2007.06.010. [3] P.J. McGovern *et al.* (2002) *JGR*, 107, 5136. [4] F. Nimmo and D. J. Stevenson (2001) *JGR.*, 106, 5085-5098. [5] J. Moores (2003) *University of Arizona Course PTYS 511*, Height concordance of Martian volcanoes over time. [6] S. Zhong (1997) *JGR.*, 102, 15287-15299. [7] G. Neukum *et al.* (1979), *LPSC*, 10th, 907-909. [8] M.H. Carr *et al.* (1984) *U.S. NASA Special Publication SP-469*, 206-263.

COMPUTER MODELING OF SOLAR ION RADIATION PROCESSING OF PLANETARY SURFACE MATERIALS. Sydney J. Chamberlin¹ and Roy Christoffersen²; ¹Department of Physics, Utah State University, Logan, Utah 84322, ²SAIC/NASA, Johnson Space Center, Houston, Texas 77058.

Introduction:

The surfaces of airless bodies in the solar system are constantly bombarded with energetic ions from the solar wind. These ions interact with solids through either inelastic (electronic) or elastic (nuclear) collisions[1]. Over time, these interactions lead to structural and chemical alterations of the solid's surface, the most common effect being the formation of amorphous rims on the surfaces of regolith grains (Fig. 1).

Basic ion transport physics allows for some understanding of the collisions underlying such damage, but fails to offer much insight into other parameters such as the width of the damaged layer and degree of amorphization over time. In addition, observational data of radiation processed grains suggest a lack of consistency in the rates of amorphization for varying materials, a peculiarity that requires better understanding based on improved integration of physical models with experimental data[2].

Space radiation processing is often investigated through experimental procedures, largely those involving the use of Transmission Electron Microscopy (TEM). It can also be modeled with Monte Carlo computer simulations. Currently, software for such modeling exists, but has never been fully exploited in space radiation processing simulations. More precise modeling with this software could apply a wider range of parameters to space radiation processing research, helping to account for factors that are harder to quantitatively predict such as the width of amorphized rims on regolith grains.

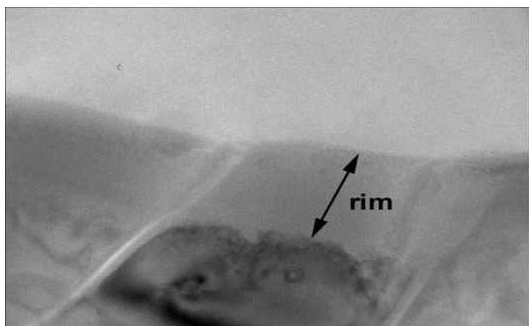


Figure 1. An amorphous rim has formed in this lunar feldspar grain, shown by arrow.

Ion Transport Software - TRIM:

Several types of software designed to complete Monte Carlo simulations exist. The best known of these is the Transport of Ions in Matter (TRIM) [3]. TRIM provides a relatively accurate assessment of a single ion impacting a target with some angle of incidence and energy, but its basic user interface fails to accommodate the range of parameters present in a plasma.

In order to make a Monte Carlo simulation for the case of the solar wind, a plasma containing ions of various energies, incident angles and species, a different interface must be used with TRIM. This interface is in the form of an array, and allows for the manual input of varying parameters. The flexibility of the array allows for any one or more of the following parameters to be varied together: ion type, energy, initial depth, lateral position, and angle of incidence.

The completion of a TRIM calculation produces several raw output files based on the array's input parameters. For space radiation processing, the most significant of these is the "E Recoil" file, which provides data on the deposition of energy from the ions into the solid. To model damage from this file, the raw deposited energy data is first converted from unit energy per depth per ion to unit energy per volume. As a function of depth, the resulting values produce a distribution of energy in the target that corresponds to damage. From this, it is straightforward to plot a damage versus depth profile for the target and predict the degree of damage the target has received.

As we are interested in the processes pertaining to the irradiation of airless bodies, the materials under investigation in the development of this model consist primarily of magnesium-rich olivine and plagioclase feldspar.

It is possible, however, to vary target surfaces in the TRIM model. Consequently, the products of a developed space radiation processing model could extend far beyond these minerals, and such a model could also find application in many areas of materials science or solid state physics.

Results of Varying Ion Angles of Incidence:

Ions in the solar wind bombard bodies in the space environment not at a constant angle of incidence, but one based on many factors such as gravitational attraction, initial velocity, electronic interactions, etc. Therefore, a first step to building a comprehensive model was to modify TRIM's input parameters for a multidirectional plasma. The input array contains three columns for the modification of ion incident angle, with each column representing a directional cosine. The values of the directional cosines are restricted to $-1 \leq \theta \leq 1$, with $\cos(x) = 1$ representing a trajectory straight into the target surface.

To randomize the directional cosines, two random numbers were generated using a random number macro. Spherical polar coordinates were then used with these angles to determine a value for each directional cosine. The angles were restricted with $0 \leq \cos(x) \leq 1$ such that all ions were constrained to hit the target.

The effect of varying ion angle of incidence in the TRIM input array is evident in the resulting damage versus depth profile (Fig. 2); it increased the amount of energy deposited at the surface of the target, placing most damage at a shallower depth. Varying angles of incidence also decreased the range of the ions. Thus, the ions caused more damage in the first depths of the target, but the width of this damaged layer did not extend as far into the solid.

Results of Varying Ion Energies:

Typical solar wind plasma consists primarily of protons and helium ions, with trace amounts of lithium and other lightweight elements; relative speeds of the solar wind range from 300 to 700 km/s [4, 5]. From this distribution of speeds, it is clear that the constituent ions of the solar wind have energies corresponding to this range.

To facilitate this energy variation in space radiation processing, it is then necessary to add a parameter to account for solar wind ion energy distributions. Utilizing a range of known ion speeds, the relative energies of the ions were determined. For each range of energies, a corresponding dose was used to find the ratios of ions of each energy, as in table 1; each ratio determined the number of ions of each energy to be used in the TRIM input array. The effect of varying ion energy, like ion angle, can be investigated via a damage versus depth profile. The input with several ion energies greatly increased the range of ions in the solid (and hence the width of the dam-

aged layer), but decreased the maximum value of energy deposited (Fig. 2). Also, it should be noted that the values of the damage curve fell off with a shallower slope than those of the control damage curve.

Table 1

Alpha Energy (keV)	Alpha Dose (ions/cm ²)	Percentage Totals (Alpha dose/Total dose)	# Ions to Input
1.2959	8.00E+11	0.001221374	31
6.2723	3.40E+13	0.051908397	1298
12.4540	1.31E+13	0.02	500
14.9811	2.57E+12	0.003923664	98
Total Ions	6.55E+14		of 25000

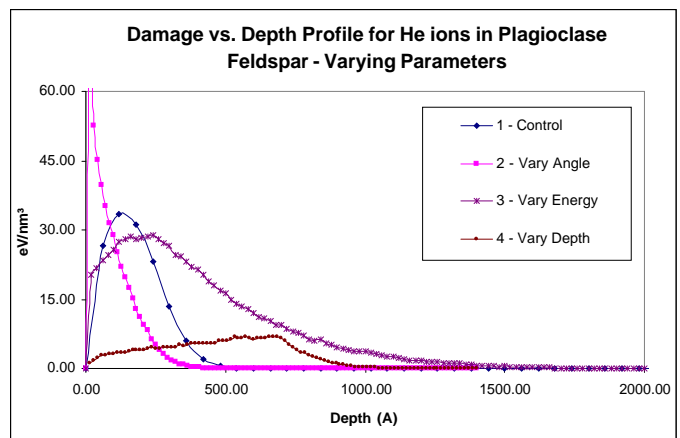


Figure 2. Damage versus depth profiles comparing the variation of different parameters. The control test did not vary any parameters.

Treatment for Sputtering:

If the energy of an ion impacting a target exceeds the solid's surface binding energy, atoms can be sputtered from the target. Sputtering causes a gradual erosion of the surface. To account for the sputtering effect in our model, the following tasks have been pursued: (a), to find a formula to calculate the sputtering rates of various materials; (b), to use this rate to calculate the effective loss of target surface; and (c), to incorporate this surface loss into the TRIM model by varying the starting depths of ions bombarding the surface. Using a predefined sputtering yield S in $atoms \cdot ion^{-1}$, the relative sputtering rate of a solid was derived as

$$R_{sp} = \frac{D \cdot S \cdot M}{N \cdot \rho}$$

where D is the ion dose in $ions \cdot cm^{-2}$, M is the atomic mass of the material in amu , N is Avogadro's number in $mole^{-1}$ and ρ is the density

of the target material in $g \cdot cm^{-3}$. This algorithm was used to determine the amount of surface that has receded for a given dose. Using this value, it was then possible to determine d_1 , the depth at which the surface has receded after some time, and to compare this to d_p , the depth of the initial damage profile. Because some of the surface containing deposited energy is eroding away, it is also necessary to calculate an adjusted dose D_{ed} to be used in finding the energy deposited. The ratio

$$\frac{d_p}{d_1} = \frac{D_{ed}}{D_{total}}$$

was derived to establish this adjusted dose.

Varying depth in TRIM calculations produced an interesting result; the maximum value of energy deposited was roughly half that of the same calculation with no depth variation, but the width of the damaged layer increased. It is also interesting to note that this result is similar to the variation of energy in terms of increasing the width of the damaged layer, but without the associated increase in total energy deposited.

Analysis with Lunar Minerals:

The TRIM model can be used along with experimental data to predict the widths of amorphous rims on lunar grains exposed to the solar wind [6,7]. To make such predictions, plagioclase feldspar and olivine samples were irradiated with ions of a single energy and angle. Using TEM procedures, a critical dose at which the samples were amorphized was determined [6,7]. This critical dose was then used with data from an identical TRIM calculation to compute the critical deposited energy E_{cd} for amorphization. In our case, we have assumed that this value is similar for both olivine and plagioclase.

The TRIM model was then used to simulate solar wind plasma, utilizing the previously discussed parameter of varying energy. Using the raw TRIM energy data, multiple damage versus depth profiles were calculated using varying doses. The depths at which the profiles reached E_{cd} are plotted for various doses (Fig. 3). From this figure, it is clear that the plasma model suggests thicker widths than that of the control case. This plasma result is in fairly strong agreement with observational data which indicates that the

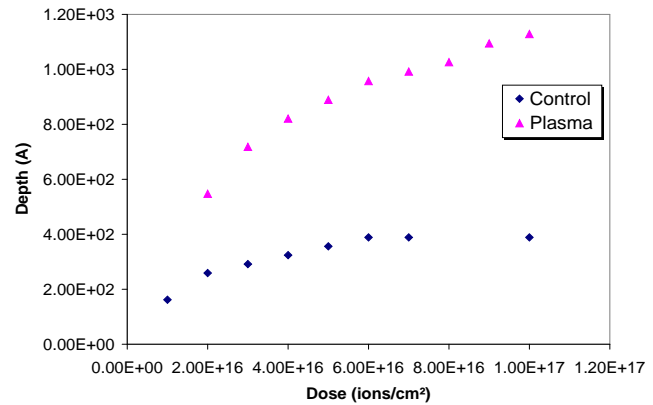


Figure 3. Predictions of the widths of amorphous rims for plagioclase feldspar as a function of dose.

amorphous rims typically range from approximately 800 to 1000 nm on these lunar grains. This also strongly correlates to the change in damage versus depth profile for varying energy, in which the damage curve decayed at a much lower rate than the control curve.

Conclusions:

A series of input data files and calculation protocols have been developed to modify TRIM for analysis of radiation processing of planetary surface materials. The new outputs consist of profiles for the amount of deposited ion collision energy in important lunar and asteroidal surface minerals, as a function of ion angle, solar wind energy distribution, and sputtering rate. Combination of the ion damage profiles with experimental results for mineral ion damage sensitivity produces results for the predicted width of radiation-amorphized rims on lunar grains that are in reasonable agreement with measured values.

References: [1] Johnson, R.E., (1965) *Physics and Chemistry in Space Planetology*, 19, 232. [2] Wang, L.M., R.C. Ewing, and W.L. Gong, (1994) *Mat. Res. Soc. Symp. Proc.*, 316, 247-252. [3] Ziegler, J.F., Biersack, J.P. and Littmark, U. (1985) *The Stopping and Range of Ions in Solids*. Pergamon Press, New York. [4] Biswas, S. and C.E. Fichtel, (1965) *Space Science Reviews*, 709. [5] Goldstein, B.E., (1998) *From the Sun, Auroras, Magnetic Storms, Solar Flares, Cosmic Rays*, 73. [6] Weber, W.J., R.C. Ewing, and L.-M. Wang, (1994) *Journal of Materials Research*, 9, 688-698. [7] Wang, L.M. and R.C. Ewing, (1992) *MRS Bulletin*, 38-44.

COOLING RATE DETERMINATION FOR H CHONDRITE IMPACT MELT BRECCIA LAP 02240. L.C. Cheek¹ and D.A. Kring², ¹Dept. of Geology, The College of William and Mary, Williamsburg, VA 23187 (lcchee@wm.edu). ²Lunar and Planetary Institute, Houston, TX 77058.

Introduction: Impact melts generated in cratering events on asteroids can provide important information regarding the collisional evolution of the solar system. In particular, the size and timing of events and the structural integrity of asteroid parent bodies can be better understood by studying the ages and cooling histories of this important class of meteorites that represents <1% of ordinary chondrite material. The purpose of this investigation is to estimate the cooling rate of H impact melt breccia LaPaz (LAP) 02240 in order to provide a context in which to interpret its thermal history.

Analytical Techniques: Petrographic properties were determined with an optical microscope.

Chemical compositions of both the melt and clast portions of LAP 02240,8 were obtained using a Cameca SX 100 electron microprobe with five wavelength-dispersive spectrometers at NASA Johnson Space Center. Silicates were analyzed using an accelerating voltage of 15 keV, a beam current of 10 nA, and a beam diameter of 1 μm . Metals were analyzed using a 15 keV accelerating voltage, 20 nA beam current, and 1 μm beam diameter.

Description and Petrography:

LAP 02240 is an H chondrite impact melt that is petrographically similar to the L5 chondrite Cat Mountain [1] and the H6 chondrite Orvinio [2]. The section (141 mm²) studied in this investigation is predominantly melt, with a small amount (9mm² and 15mm²) of clastic material along each of two edges. Ar-Ar dating indicates that the melt fraction was generated ~3900 Ma [3] and therefore may be linked to a cataclysmic bombardment that affected the inner solar system [4, 5]

Impact Melt. Point counts were made of the distribution of silicate, metal, and sulfide phases in the melt. A total of 1720 points spaced 198 μm apart indicate that the melt consists of 86% silicate material and 14% metal and sulfide phases. The silicate portion is predominately (80%) a matrix of fine-grained (<40 μm) olivine (Fa₁₇) and pyroxene (Fs₁₅) that are in equilibrium. Larger (40 to 590 μm) olivine and pyroxene xenoliths and xenocrysts comprise the remaining 20% of the silicate phases (Fa₁₈, Fs₁₆) (Fig 1a).

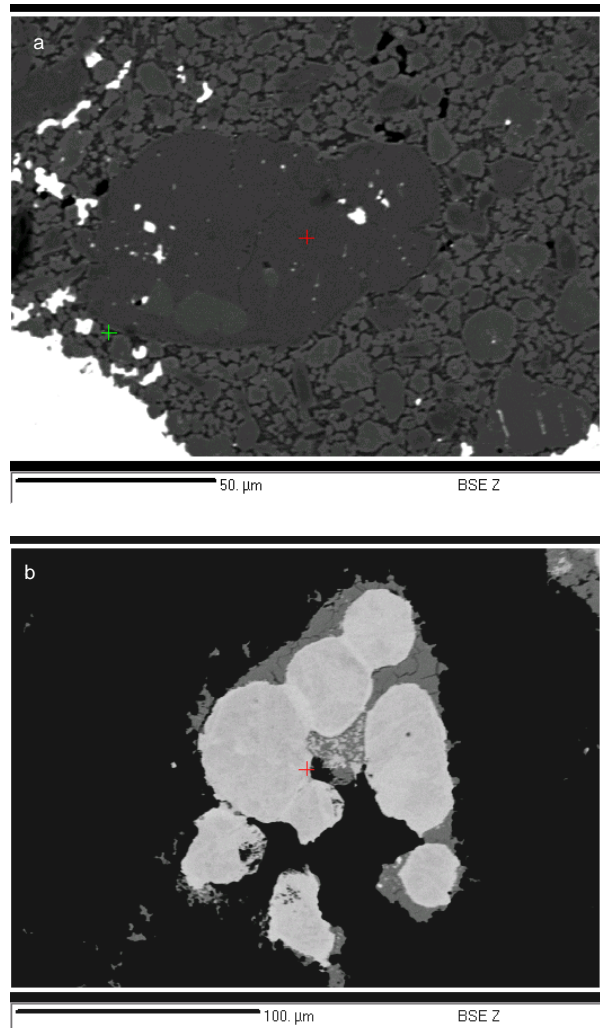


Fig. 1. Backscattered electron images of textures in the impact melt matrix. (a) Matrix of olivine and pyroxene. Many grains show brighter rims, but their narrow widths prevented reliable compositional analyses. Interstitial material was not analyzed due to the small grain size. (b) Metal sulfide assemblage within the melt matrix. Brightness and contrast have been adjusted so that the silicate material is undersaturated and appears black.

The metal is dominated by relatively low Ni compositions (5.82-14.47 wt% Ni) and typically occurs as rounded orbs surrounded by sulfide (troilite). These metal/sulfide assemblages occur both in isolation and as complex aggregates containing multiple metallic orbs (Fig. 1b). Individual orbs range up to 115 μm in size, although small (<10 μm), finely disseminated

particles also occur in the troilite around orbs. The largest metal/sulfide aggregates range up to 570 μm . The metal and sulfide phases show a bimodal size distribution, with the majority of particles having diameters $\leq 1 \mu\text{m}$ or between 59 and 151 μm (Fig. 2).

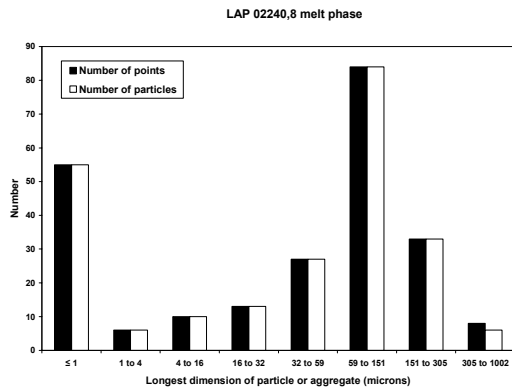


Fig. 2. Histogram of point count analyses and particle sizes of metal and sulfide in the melt phase.

Automated linescans across metal orbs show an increase in Ni content toward the rims (up to 14.47 wt%) (Fig. 3). The metal also contains 0-1.9 wt% P, although phosphide particles were not identified. According to Doan and Goldstein [6], P concentrations of $> 0.1 \text{ wt}\%$ are sufficient to affect growth processes in the metal. Romig and Goldstein's [7] Fe-Ni (P-saturated) phase diagram was therefore used in our assessment of the metal.

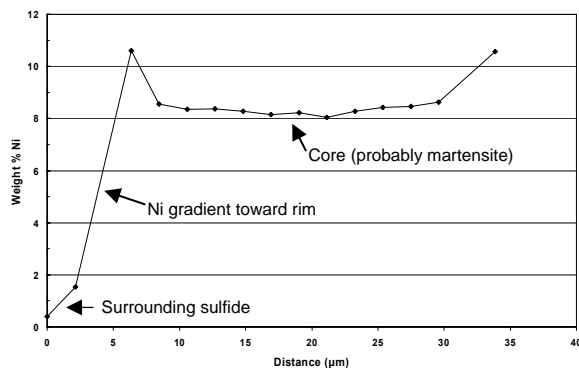


Fig. 3. Typical Ni profile across a metal grain. The Ni content of the core is relatively homogenous, but is enriched near the grain margin which is surrounded by troilite.

Estimated Cooling Rates: The melt portion of LAP 02240 records evidence for two episodes of cooling. The first (stage 1) corresponds to the brief period during which the superheated melt was thermally equilibrating with relatively cool clast material. In chondritic impact melts, this stage corresponds to tem-

peratures of approximately 1400 to 950 $^{\circ}\text{C}$ [8], and can be quantified based on metallographic textures. The second (stage 2) represents the rate at which the subsolidus breccia slowly conducted and/or radiated heat to its surroundings on the asteroid parent body. This rate can be estimated by comparison of Ni gradients with other slowly-cooled chondritic meteorites.

Stage 1 rapid cooling. The cooling rate during thermal equilibration affects the nucleation and growth of metal. Thus, the spacings of adjacent metallic cells and individual cell widths were measured following the method of Blau and Goldstein [8] and Scott [9]. The average cell spacing in 12 metal assemblages is 30, 33, 36, 37, 37, 38, 40, 43, 43, 43, 44, and 45 μm , corresponding to cooling rates of 8.6 to 27.3 $^{\circ}\text{C}/\text{s}$. The average cell width in 18 metal assemblages ranges from 20 to 50 μm , reflecting cooling rates of 6 to 84 $^{\circ}\text{C}/\text{s}$. These rates are comparable to those for the meteorites Dimmitt (H4), Pulsora (H3-7), Tell (H6), Tynes Island (H3-6), and Weston (H3-6) [9].

Stage 2 slow cooling. Ni gradients in metal indicate fractionation during solidification of the impact-melted metal-sulfide liquids. These gradients confirm that the liquids were not quenched (thus preserving homogeneous compositions), but were cooled slowly enough for fractionation to occur with falling temperature.

The survival of the gradients also indicate that subsequent cooling was sufficiently fast that they were not erased. Since longer cooling times or slower cooling rates would be expected to level out the Ni profiles, steeper gradients should be consistent with faster cooling rates. This has been demonstrated experimentally [10], and therefore rim gradients may be used as a semi-quantitative estimate of cooling rate.

The Ni profiles for both Ramsdorf (L6) and Orvinio (H6) are similar to those for LAP 02240. Smith and Goldstein [10] estimated the cooling rate for Ramsdorf as 100 $^{\circ}\text{C}/\text{day}$ ($10^{-3} \text{ }^{\circ}\text{C}/\text{s}$) based on structural similarities with experimentally heat-treated samples (heated to 1250 $^{\circ}\text{C}$, cooled at 100 $^{\circ}\text{C}/\text{day}$) and semi-quantitative cooling rate criteria. For Ramsdorf, these criteria include high Ni content in troilite (0.11 wt%) and steep rim gradients (from 8 to 20 wt%), which both indicate relatively fast cooling. Orvinio also shows relatively high rim gradients (from 1 to 8 wt%), but its Ni content in troilite is slightly lower than for Ramsdorf (0.08 wt%). They therefore inferred the cooling rate for Orvinio to be 100 $^{\circ}\text{C}$ to 15 $^{\circ}\text{C}/\text{day}$ (approximately 10^{-3} to $10^{-4} \text{ }^{\circ}\text{C}/\text{s}$). In our sample, rim gradients (from 2 to 6 wt%) are similar to those in Orvinio. This suggests a cooling rate of approximately 10^{-3} to $10^{-4} \text{ }^{\circ}\text{C}/\text{s}$ for LAP 02240.

If the cooling rate was sufficiently slow, then secondary kamacite grows along an orb's margin. This was observed in the reheated chondrites Cat Mountain,

Wickenburg, Farmington, Rose City, Lubbock, and Arapaho) [1, 9]. LAP 02240 does not have detectable bands of secondary kamacite ($< 1 \mu\text{m}$ wide), indicating that cooling rates were faster than 10^{-7} to $10^{-10} \text{ }^\circ\text{C/s}$, the rates derived for the L chondrites (and the H chondrite Rose City) shown in Figure 4. This is consistent with the rate of 10^{-3} to $10^{-4} \text{ }^\circ\text{C/s}$ suggested above by comparison with Orvinio. Such a rapid cooling rate implies a relatively shallow burial depth, likely in the melt breccia lens, the crater walls, or the ejected material.

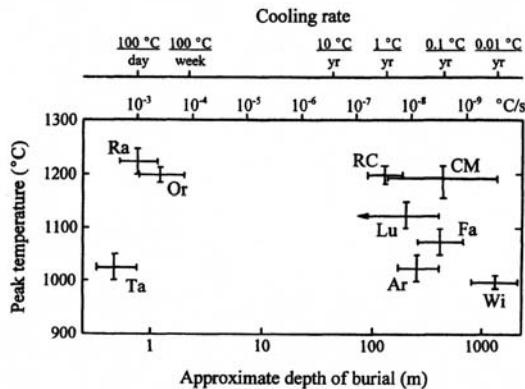


Fig. 4. The approximate depth of burial of impact melt breccia LAP 02240 as inferred from the metallographic cooling rate [modified from [9, 1]. Also plotted on the diagram are similar calculations for Ramsdorf (Ra), Orvinio (Or), Tadjera (Ta), Rose City (RC), Lubbock (Lu), Farmington (Fa), Arapahoe (Ar), and Wickenburg (Wi). All are L-chondrites with the exception of LAP 02240, Orvinio, and Rose City.

Conclusions. Melt breccia LAP 02240 appears to have cooled at rates comparable to other H chondrites throughout both stages of its cooling history. During high-temperature thermal equilibration the melt cooled at 6 to 84 $^\circ\text{C/s}$. Subsolidus cooling occurred at a rate of 10^{-3} to $10^{-4} \text{ }^\circ\text{C/s}$. The latter estimate suggests that LAP 02240 was formed at relatively shallow depths on the asteroid parent body.

Acknowledgements: Many thanks to Loan Le at NASA JSC for all of the help with the microprobe. Thanks also to the LPI summer intern program.

References: [1] Kring, D.A. et al. (1996) *J. Geophys. Res.*, 101, 29, 353-29, 371; [2] Grier, J.A. et al. (2004) *Meteoritics and Planetary Science*, 39, 1475-1493; [3] Swindle, T.D. et al. (2006) *Lunar Planet. Sci.*, XXXVII, #1454; [4] Bogard, D.D. (1995) *Meteoritics*, 30, 244-268; [5] Kring, D.A. and Cohen, B.A. (2002) *J. Geophys. Res.*, 10 (E2), 10.1029/2001JE001529; [6] Doan, A.S., and Goldstein, J.I. (1970) *Met. Trans.*, 1, 1759-1767; [7] Romig, A.D. Jr., and Goldstein, J.I. (1980) *Met. Trans.*, 11A, 1151-1159; [8] Blau, P.J., and Goldstein, J.I. (1975) *Geochim. Cosmochem. Acta*, 39, 305-324; [9] Scott, E.R.D. (1982), *Geochim. Cosmochem. Acta*, 46, 813-823; [10] Smith, B.A. and Goldstein, J.I. (1977) *Geochim. Cosmochim. Acta*, 41, 1061-1072.

A PARAMETRIC GEOELECTRICAL MODEL OF THE MARTIAN NORTH POLAR LAYERED DEPOSITS; J. Cosmidis¹, E. Heggy², S. M. Clifford²; A. Humeau³; ¹Ecole Normale Supérieure, Lyon, France; ²Lunar and Planetary Institute, Houston, 77058 TX, USA; ³Université de Bordeaux I, Pessac, France

Introduction: Since the earliest telescopic observations of Mars, the bright white caps visible at both poles of the planet have been among the most striking features. During wintertime, the Martian polar caps are covered by a thin CO₂-ice layer which sublimates away by the end of spring. In the North, the seasonal CO₂ frost total dissipation reveals a much smaller residual cap mainly composed of water-ice and atmospheric dust depositions. High-resolution images of the spiral scarps that run through the cap have revealed the presence of finely layered deposits. The variations in thickness and albedo of the layers are thought to reflect the variations in the relative abundance of dust and water-ice deposited in the cap. As interaction between ice and atmosphere is a basic component of the Martian climate, the North Polar Layered Deposits (NPLD) could preserve a record of the seasonal and climatic cycling of atmospheric CO₂, H₂O and dust over the past $\sim 10^5$ - 10^8 years. For this reason, they may serve as a Rosetta Stone for understanding the geological and climatic history of the planet [1].

The orbital radar sounders SHARAD (SHallow RADar) and MARSIS (Mars Advanced Radar for Subsurface and Ionosphere Sounding) have the ability to probe the Martian subsurface to kilometers depth, providing a three-dimensional view of the polar caps. The radar observations can be interpreted in terms of internal geometry and thickness of the deposits, topography of their interface with the underlying plains, and perhaps presence of basal melt water. However, the accuracy of these interpretations depends on our ability to constrain the dielectric properties of the polar ices. Indeed, the dielectric constant of the ice controls the way the electromagnetic wave interacts with the subsurface materials and is essential to evaluate the performance of the radar instruments.

In this paper, we construct first order modeled maps of the surface dielectric properties of the NPLD. We first derive recent Mars Global Surveyor Thermal Emission Spectrometer (TES) thermal inertia observations [2] in order to draw a map of the dust mass fraction in the ice at the top of the permanent cap. Then we use laboratory measurements of the dielectric

properties of Martian polar ice analogs with various temperatures, radar frequencies and mass fractions and compositions of dust in order to obtain the parametric dielectric maps.

Performing the modeled dust map of the surface of the NPLD: Thermal inertia is a material property controlling planetary diurnal surface temperature. It is defined by the relation $I = \sqrt{\rho C k}$ (J.m⁻².K⁻¹.s^{-1/2}) where ρ is the bulk density of the material, C its specific heat capacity and k its bulk thermal conductivity. The thermal conductivity and thus the thermal inertia of an icy soil is primarily controlled by its physical properties, such as particle size, porosity, and pore connectivity, within the top few centimeters of the subsurface. The thermal inertia is also a function of the dust concentration in the ice.

In this section, we describe the thermo-physical model we developed to obtain a theoretical relation between thermal inertia and the dust weight fraction of an ice-dust mixture at given temperature, porosity and pore size of the ice. We have calculated the bulk specific heat capacity as $C = \tau C_d + (1 - \tau) C_i$ where τ is the weight fraction of dust and C_i and C_d are the specific heat capacities of ice and dust respectively. Assuming a low dust contamination, the bulk density is:

$\rho = (1 - \Phi)[(1 - \varphi)\rho_i + \varphi\rho_d]$ where ρ_i and ρ_d are the densities of ice and dust respectively, Φ the porosity and φ the dust content by volume. In order to take into account both the effect of heat conduction within the solid particles and across interparticle contacts and the effect of heat conduction by the vapor present in the void space between the particles, the bulk thermal conductivity is calculated as $k = k_s + \Phi k_v$, where k_s and k_v are the thermal conductivities of the icy matrix and the pores respectively. We use $k_s \sim k_i$ the thermal conductivity of ice and k_v as a complex function of the ice physical and geometrical parameters obtained by thermal modeling of the vapor flux in the pores [3].

The calculation of thermal inertia given by this model for different temperatures, pore

radius, porosities and dust weight fractions shows that Φ and τ are the main parameters controlling the variations thermal inertia. In particular, low porosities and dust content of the ice increase thermal inertia. Our study demonstrates a simple polynomial relation between τ and I for a constant porosity and for low dust concentrations.

Thermal inertia maps have been derived from recent TES observations of the surface temperatures of Mars taken over three Mars-years from orbit 1583 to 24346 [2]. We use these data to draw the map of the dust contamination of the ice at the surface of the NPLD (Fig.1). An assumption about the maximum value of dust weight fraction in the ice is necessary to produce a map consistent with TES results. Langevin *et al* (2005) suggest an upper limit to dust content by volume of 6% which corresponds to a dust weight fraction of ~15%. Though, much smaller upper limit values are possible [4].

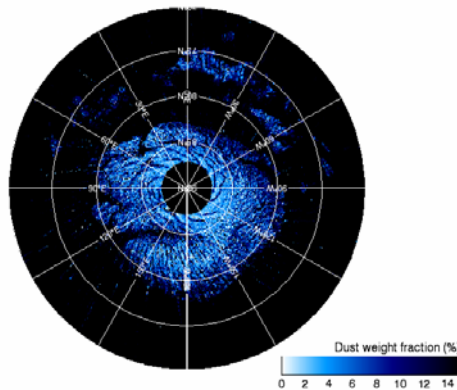


Figure 1: Dust contamination map of the NPLD, assuming an upper limit to dust weight fraction in the ice of 15%.

Relation between dust weight fraction and the dielectric parameters of ice-dust mixtures: We have conducted laboratory measurements of the dielectric properties of ice-dust mixtures with various concentrations of Martian basaltic soil analog as a function of density, temperature and radar frequency range (see Humeau *et al.*, this volume). The results show an increase in the dielectric constant as a function of dust content. The measurements indicate that the influence of temperature is not as significant as dust content on the real and complex parts of the dielectric constant. The dielectric properties of the ice-dust mixtures appear to be approximately frequency-dependant.

Fig. 2 represents the empirical relation derived from previous measurements of the real

part of the dielectric constant and the loss tangent as function of the dust weight fraction [Heggy, 2007, *in press*].

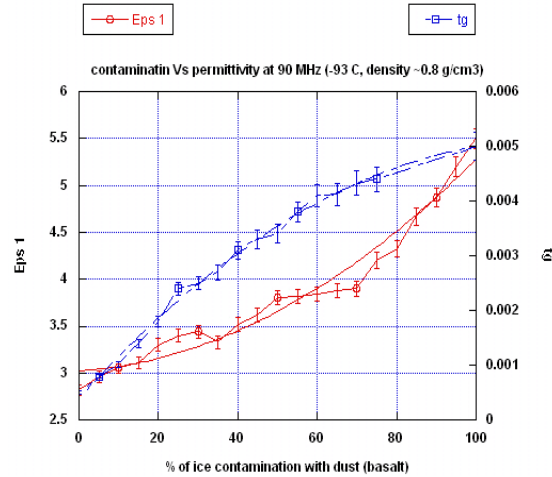


Figure 2: Real part of the dielectric constant and loss tangent of ice-basaltic dust mixtures as functions of the dust weight fraction for a constant temperature of 180K and a frequency of 90MHz.

Parametric dielectric maps: We have integrated the laboratory measured dielectric properties and the TES thermal inertia data into a comprehensive first order model of the surface dielectric properties of the PLD. We have obtained maps of the real part of the dielectric constant (Fig. 3) and of the loss tangent at given surface temperature, porosity of the ice, dust composition and radar frequency.

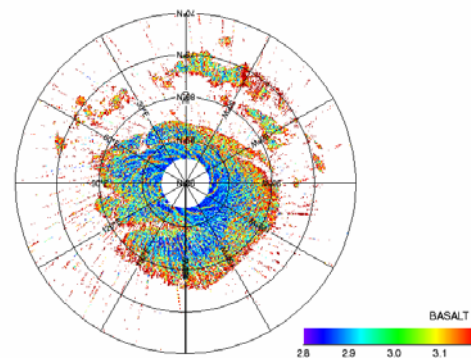


Figure 3: Real part of the dielectric constant at the surface of the NPLD at 90 MHz, assuming a basaltic composition of the dust and homogeneous surface temperature and porosity.

The equation giving the penetration depth as a function of the real and imaginary parts of the dielectric constant can be found in Heggy (2006) [5]. We have produced theoretical penetration depth maps at appropriate MARSIS and SHARAD frequencies (2MHz and 20MHz

respectively) (Fig. 4a and 4b), assuming that the dielectric properties observed at the surface don't vary significantly in depth. These maps show maximal values since their calculation don't take into account the layering inside the cap which causes energy losses and reduces the penetration depth. MARSIS radar waves have maximal penetration depths up to ~25km whereas SHARAD waves shouldn't be able to penetrate the PLD deeper than ~4000m in the ice cap.

The thickness of the NPLD is approximately equal to their elevation above the surrounding plains. Hence, the maximal thickness is just over 3km at the pole and decreases equatorward. Our model demonstrates that both MARSIS and SHARAD have the capability to detect the interface between the icy material constituting the layered deposits and the underlying basaltic terrains. Radargrams of the NPLD from MARSIS [6] and SHARAD [7] have shown basal reflectors at depths estimated to ~2km and >1km respectively, which seems to confirm our predictions.

Conclusion and prospects: The first-order geoelectrical model of the NPLD presented in this effort has produced estimates consistent with recent radar observations from MARSIS and SHARAD orbital sounders. The velocity of a radar wave propagating in a geologic material depends on its dielectric properties. Thus, knowing the value of the dielectric constant of the NPLD materials is necessary to convert time-scales into depth-scales and quantitatively interpret the radar observations of the base of the NPLD in terms of ice thickness. This should be valuable to assess the volume of ice stocked in the polar cap and constrain the amount of lithospheric flexure due to its load.

Thermal observations of the layering visible in the troughs that run through the North cap coupled with MOLA (Mars Orbiting Laser Altimeter) topographic data will allow us to perform a three-dimensional model of the dielectric properties of the NPLD materials and improve the precision of the interpretation of radargrams from present and future Martian missions.

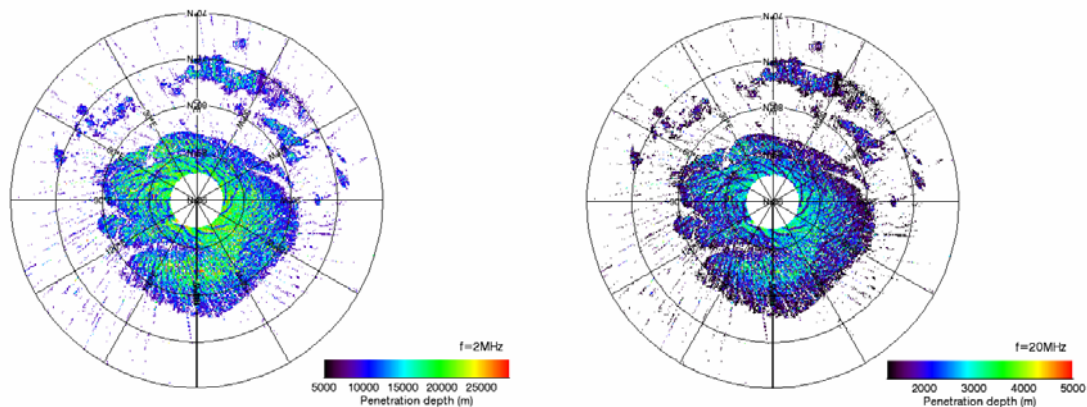


Figure 4: Theoretical radar penetration depths at MARSIS (4a) and SHARAD (4b) frequencies

References: [1] Clifford, S. M. (2000), *Icarus* 144, 210-242 [2] Putzig, N. E., (2007) *Icarus*, in press [3] Clifford, S. M., (1993), *JGR* 98, 10,973-11,016 [4] Langevin, Y. (2005), *Science* 307, 1581-1584 [5] Heggy, E. (2006), *JGR* 111 [6] Picardi, G. (2005), *Science* 310, 1925-1928 [7] Phillips, R. J. (2007), *LPSC* 38

DIFFERENTIATION OF THE HED PARENT BODY. H. Elkonton¹, J. Jones², ¹Department of Earth and Environment, Mount Holyoke College, 50 College St, South Hadley, MA 01075, hdelkint@mtholyoke.edu, ²KR, NASA/JSC Houston, TX 77058.

Summary: Melting experiments were performed on the Righter-Drake HED parent-body bulk composition at temperatures and pressure appropriate for eucrite formation. MELTS calculations were also performed using experimental conditions. Comparison of these two data sets will provide insight into the accuracy of MELTS for modeling the thermodynamic conditions of these extra-terrestrial materials.

Introduction: The HED meteorites (howardites, eucrites and diogenites) are a group of meteorites thought to originate from the same parent body. This parent body is assumed to be 4 Vesta, whose surface has a eucrite-like composition [1]. Eucrites are relatively simple basalts, and diogenites are pyroxene cumulates. The assumption that these two types of meteorites are related is fueled by the existence of the howardites, which are breccias made up of both eucrite and diogenite clasts. In order to prove the relationship between the eucrites and diogenites, several different models have been proposed to provide a setting in which they could evolve together. The two most prevalent ideas are those of fractional crystallization and partial melting. The former suggests that eucrites are an end product and that cumulate eucrites and diogenites are the cumulates; the latter that different degrees of melting are thought to have formed various eucrites [2].

Recently, Righter and Drake proposed a model which they believe reconciles issues of timing and other physical conditions that previous models have failed to address. They envision a scenario in which eucrites and diogenites form during the equilibrium crystallization of a magma ocean present on the HED parent body [3]. Accordingly, they have modeled this crystallization history using MELTS and MAGPOX/MAGFOX, two thermodynamic modeling programs.

The primary focus of our research was to run experiments in the laboratory that were comparable to those of Righter and Drake's

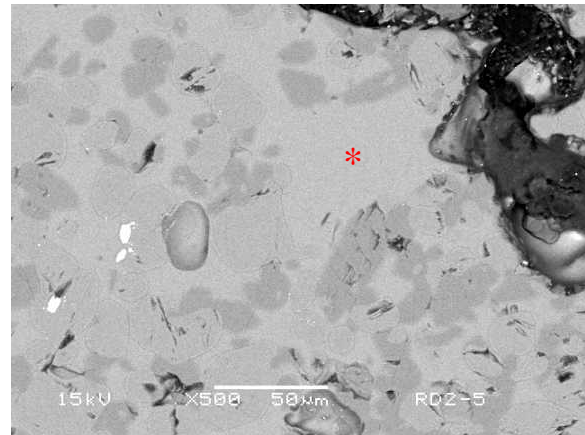


Figure 1. SEM backscatter image of experiment RD2-5, run at 1225°C for ~96 hrs. Note the large melt pocket (marked by an asterisk), dark pyroxene crystals, larger moderately shaded olivines, and bright white chromites.

model. The data will then be used to evaluate the ability of MELTS to reproduce the results of experiments run at the same conditions.

Experiments: The composition used was that specified by Righter and Drake as their chosen bulk composition for the HED parent body, or .70 L and .30 CV chondrites [3]. Experiments were run for three to eight days (varied to approach equilibrium), two charges per run, in a 1-atm Deltech furnace at iron-wüstite oxygen fugacity. Experiments were hung on Re loops to prevent iron-loss, and were rapidly drop-quenched to minimize quench effects. Temperature steps used were 1180°C, 1200°C, 1225°C, 1250°C. 1180°C is Stolper's original proposed eucrite liquidus [2], and 1250°C is the Righter-Drake model temperature at which equilibrium crystallization gives way to fractional crystallization [3]. The two intermediate temperature steps (1200, 1225°C) were chosen to provide a continual set of data.

MELTS calculations were also conducted to compare to the experimental data [4], [5]. These calculations were run using the same temperatures, pressure and oxygen fugacity as used above. The bulk composition was that of Righter-Drake, but adjusted for estimated Na-loss that experiments underwent during partial melting.

Analysis: Experiments were imaged in back-scatter on the 5910LV SEM to locate viable melt-pockets for analysis. Melt-pockets were no larger than 50 microns at the highest melting temperatures, and no melt-pockets smaller than 10 microns were analyzed at the lowest temperatures. Experiments were analyzed on the Cameca SX100 electron microprobe with a 5 micron beam at 15 kV. For each analysis of a melt pocket, analyses were taken for adjacent olivine and pyroxene crystals.

Data from the microprobe was used to check the stoichiometry of olivine, as well as to calculate the average compositions of all the phases, partition coefficients (both measured and expected), and Fe/Mg K_D s (to evaluate equilibrium). Modes were calculated using Ca-Mg-Al-Si (CMAS) balance. These modes were then used to confirm that no Fe had been lost from the system.

Following the acquisition of MELTS data, calculations were run for MELTS and experimental data using their respective modes and average phase compositions to ensure that there was mass balance, and that original bulk compositions could be recovered.

Results and Discussion: Calculations for olivine stoichiometry were extremely good, indicating that the microprobe analyses were well calibrated. Fe/Mg K_D s were also as expected (~.33 for olivine and ~.29 for

pyroxene), indicating that equilibrium had been approached during partial melting in the furnace. Figure 2 shows average K_D values at given temperatures for olivine and pyroxene, using both experimental and MELTS values.

Thus, we have established that the experiments and analyses were valid, and that MELTS can approach experimental equilibrium. Agreement between the compositions of the phases produced experimentally and with MELTS was also checked; this revealed consistent agreement between the two methods as each temperature step. To better illustrate this, a delta (δ) value was calculated for major oxides in the three major phases at each temperature step:

$$= ({}^iC_{\text{meas}} - {}^iC_{\text{MELTS}}) / {}^iC_{\text{meas}} * 100$$

where i is the major oxide (MgO, SiO₂, FeO, CaO or Al₂O₃), and C is the wt. % oxide, as measured experimentally or produced by MELTS. Figure 3 is a representative graph for the 1180°C run. As can be seen in this figure, the agreement between experimental results and MELTS calculations is quite good for the elements Mg, Si and Fe, with δ 5% relative. Al, a major constituent of the melt phase, also shows this level of agreement between experimental and MELTS results. The only significant discrepancy is with Ca, with δ 10%

relative. These observations are true of all four temperature steps. Slight discrepancies between experimental values and MELTS values are usually the result of MELTS allotting these oxides to a minor spinel phase. This phase is noted in images taken of experiments (see Figure 1), but was not analyzed due to size constraints.

Mode calculations took a departure from the expected trends, based on the results of Righter and Drake. Although it had been anticipated that the modal pyroxene would increase consistently with a decreasing temperature, this proved not to be the case. The three phases (pyroxene, olivine

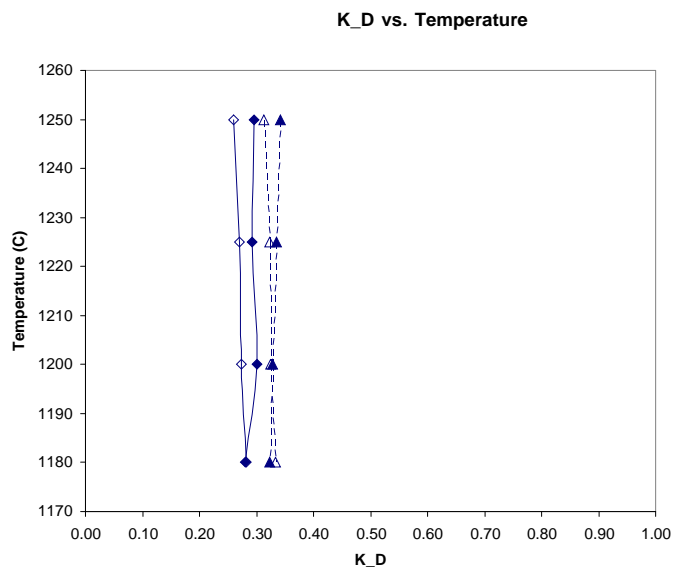


Figure 2. Graph showing Fe/Mg K_D versus temperature for both experimental and MELTS results.

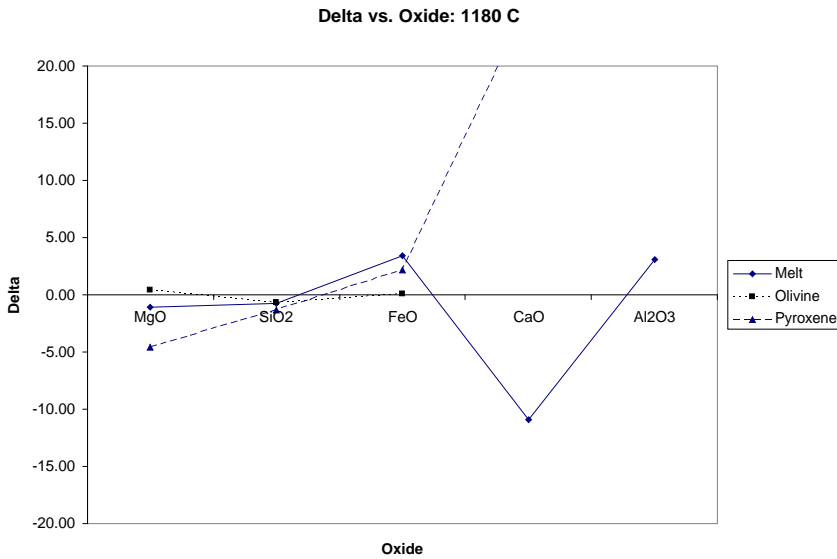


Figure 3. Graph showing delta for various major oxides present in the three major phases: melt, olivine and pyroxene.

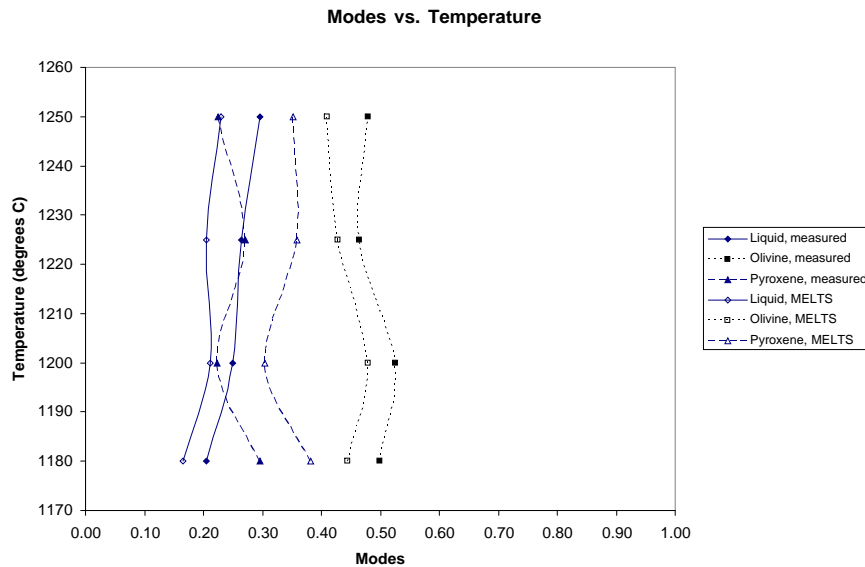


Figure 4. Graph showing modes versus temperature for both experimental and MELTS results.

and melt), have relatively constant proportions across the temperature gradient, possibly due to the increasing Na content as temperature decreased and less Na was volatilized.

Modes were calculated using three methods: in addition to the analytical CMAS mass balance and MELTS calculations, a least squares method was also employed [6]. All three methods yielded similar melt fractions; however, the analytical method consistently underestimated pyroxene compared to the other

two methods. The reason for this is still under investigation.

Conclusions: MELTS appears to approach good equilibrium and does an excellent job of predicting phase compositions for this experimental composition. Phase proportions are less certain, and further research into this matter needs to be done. To this end, element maps have been made using the electron microprobe to get more absolute modal values for our experiments. This new data is in the process of being analyzed. Results from this may shed light on the discrepancy.

Overall, the data implies that Righter and Drake's conclusions based on MELTS seem to be corroborated.

Acknowledgements:

I would like to thank Loan Le for all of her help while we were running and analyzing our experiments— things would not have gone so smoothly without her. I would also like to thank Dr. Justin Filiberto for his help running MELTS, and for running Iqpet calculations for us. Finally, I would like to thank Georg Ann Robinson for her patience while I mapped my experiments, and for always finding a way to fit me in for SEM time.

References: [1] TL Grove and KS Bartels. (1992) *Proceedings of Lunar and Planetary Science*, 22, 437-445. [2] E Stolper. (1977) *Geochimica et Cosmochimica Acta*, 41, 587-611. [3] K Righter and MJ Drake. (1997) *Meteoritics & Planetary Science*, 32, 929-944. [4] MS Ghiorso and RO Sack. (1995) *Contributions to Mineralogy and Petrology*, 119, 197-212. [5] PD Asimow and MS Ghiorso. (1998) *American Mineralogist*, 83, 1127-1131. [6] MJ Carr. (2000) *Iqpet for Windows*. Terra Softa Inc., Somerset, N.J.

PARAMETRIC ELECTROMAGNETIC CHARACTERIZATION OF ICE-DUST MIXTURES, TO SUPPORT THE MARSIS DATA ANALYSIS OF THE MARTIAN POLAR LAYERED DEPOSITS (PLD); Alexis Humeau¹, Essam Heggy^{2,4}, Stephen Clifford², Jean-Louis Miane³; ¹University of Bordeaux 1, Talence, France; ²Lunar and Planetary Institute, Houston, TX, USA; ³Laboratoire IMS, Pessac, France; ⁴Institut de Physique du Globe, Paris, France.

Introduction: Since early 2004, the low frequency (1-5MHz) orbital sounding radar, MARSIS (Mars Advanced Radar for Subsurface and Ionosphere Sounding) on board Mars Express spacecraft (European Space Agency - ESA), has been continuously providing new insight on the Martian subsurface, searching for potential water aquifers, and exploring the subsurface stratigraphy, particularly in the polar layered deposits. The accuracy of the subsurface mapping and the penetration depth of the radar waves in the soil are strongly associated to the geoelectrical properties of the shallow subsurface. The presence of relatively conductive materials, such as iron oxides in mafic dusts, can significantly decrease the penetration depth [1,2]. The geographical and vertical distribution of those materials is yet poorly known on Mars. This raises several ambiguities about the geoelectrical properties of the Martian subsurface, especially ice-dust mixtures (also referred to as dirty-ice). Dirty-ices are very complex dielectric systems with their relative permittivity depending on the temperature, the dust composition, the presence of unfrozen water in the ice and the radar wave frequency.

Scientific Objectives: A good knowledge of the dielectric properties of Mars analog terrains is crucial for quantitative analysis and interpretation of the MARSIS data. Experimentally characterizing these analogs results in better understanding MARSIS radargrams in term of quantifying the penetration and deducing the electromagnetic characteristics of the Martian subsurface. Moreover, the experimental lab results will be integrated in parametric geoelectrical models of the Martian surface and subsurface (J. Boisson and J. Cosmidis – LPI summer internships 2007). Our primary objective is to study dirty-ices, which are mixtures of different Mars analog materials and water, cooled at negative temperatures. For each mixture, we measure the real part, ϵ' , of the dielectric permittivity and the loss tangent, δ .

$$\epsilon = \epsilon' - j\epsilon'' \text{ and } \tan \delta = \frac{\epsilon''}{\epsilon'}$$

The measurement's results allow us to understand the effect of the dust composition, the percentage of dust in the mixture, the temperature and the frequency on the dirty-ice dielectric properties.

Measurement Setup: To measure the dielectric permittivity of dirty-ices, we use an impedance analyzer (Agilent – E4991A), an open-ended coaxial line and an environmental chamber which can be cooled down to -70°C . The cell we use is assimilated to a capacitance, C , whose value depends on the permittivity ϵ of the studied mixture: $C = C_0 \cdot \epsilon^b$ where C_0 and b are two coefficients depending on the cell geometry and that are known.

The analyzer provides the sample impedance Z . In order to characterize a mixture we have to perform a measurement on a reference sample which is the air (Z_{air}) and then compare its impedance to the sample under study (Z_{sample}). From these impedances, we can calculate the reflection coefficient, ρ , so that we obtain the following ratio:

$$\frac{\rho_{\text{sample}}}{\rho_{\text{air}}} = \frac{\frac{1}{Z_0} - \frac{1}{Z_{\text{sample}}}}{\frac{1}{Z_0} + \frac{1}{Z_{\text{sample}}}} \times \frac{\frac{1}{Z_0} + \frac{1}{Z_{\text{air}}}}{\frac{1}{Z_0} - \frac{1}{Z_{\text{air}}}}$$

Where $Z_0=50\Omega$, is the characteristic impedance of the coaxial line.

Finally, we calculate the permittivity of the studied mixture, as a function of frequency:

$$\epsilon = \sqrt[b]{\frac{1 - \frac{\rho_{\text{sample}}}{\rho_{\text{air}}} \times \frac{1 - j\omega C_0 Z_0}{1 + j\omega C_0 Z_0}}{j\omega C_0 Z_0 \left(1 + \frac{\rho_{\text{sample}}}{\rho_{\text{air}}} \times \frac{1 - j\omega C_0 Z_0}{1 + j\omega C_0 Z_0} \right)}}$$

Where ω is the angular frequency.

All the calculations are made using an IDL program that provides a 4 column array with the frequency, the real and imaginary parts of ϵ and the loss tangent.

To perform the measurement, we place the open-ended coaxial line in the environmental chamber, and we connect it to the analyzer via an insulated cable. The most important steps of a measurement are the calibration of the

analyzer and the temperature compensation. The first one aims at defining a reference plane where the measurement accuracy is specified, whereas the second one, whose effectiveness is strongly dependent on the calibration process accuracy, is used to minimize the effects of the low temperature on the phase of the measured impedance. When these two steps are made, we proceed to the air and sample measurement and then to the permittivity calculation using IDL. As the surface of Mars has been mainly identified as volcanic material [3,4], the mixtures we studied were made of different contaminations (from 1% to 75%) of very small grains (<50 μ m) of basalt or others Mars-like dusts, mixed in ice, for temperatures going from -20°C to -70°C, on the frequency range 1-500 MHz that cover both MARSIS and SHARAD acquisition frequencies.

Laboratory Results: Here, we present some of the results we obtain during the lab measurements. For each sample, we calculate the real part of the permittivity and the loss tangent as functions of frequency. The experiments aim at demonstrating the effects of temperature (1,2), dust contamination (3) and type of dust (4) on the dirty-ice's dielectric properties.

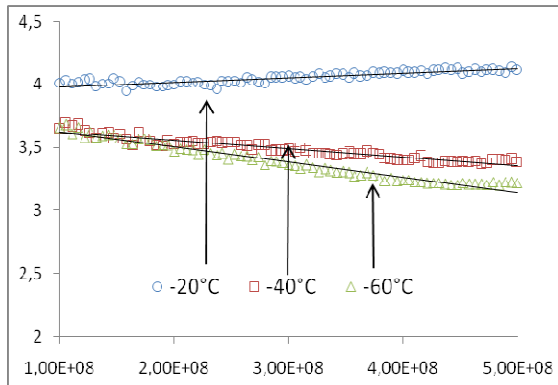


Figure 1: ϵ' as a function of temperature and frequency, for a 50% basalt and 50% ice mixture.

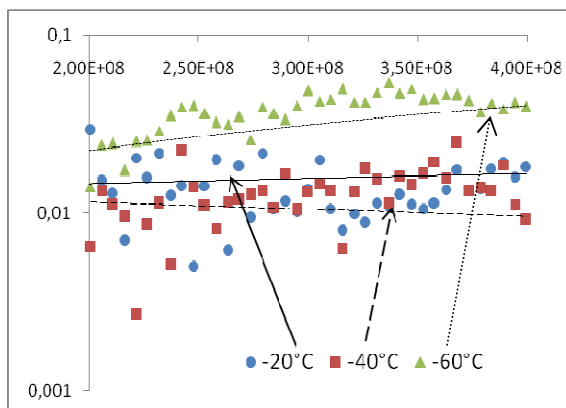


Figure 2: Tan delta, in logarithmic scale, as a function of temperature and frequency, for a 50% basalt and 50% ice mixture.

Figure 1 shows the evolution of the real part of the permittivity for a 50% basalt and 50% ice mixture, at three different temperatures on the frequency range 100 to 500MHz. For the three temperatures, -20, -40 and -60°C, the evolution of ϵ' as a function of the frequency is linear and nearly constant on this range. Hence we can expect that the evolution of the loss tangent will mostly depend on the imaginary part, ϵ'' . On figure 1, ϵ' is 4 at -20°, 3.5 at -40° and goes from 3.6 to 3.2 at -60°C. This difference is due to the presence of unfrozen water in the ice matrix for temperatures approaching the zero freezing point: as the amount of unfrozen water in the sample mass is higher at -20°C than at -60°C, and as the water permittivity is high ($\epsilon=80$), the permittivity of ice is higher at -20°C than at -60°C.

Figure 2 shows the evolution of loss tangent, on a logarithmic scale, for three different temperatures on the frequency range 200 to 400MHz. This parameter is linear and relatively constant on those frequency and temperature ranges. The observed losses are more important at -60°C (0,02) than at -20°C (0,005) and -40°C (0,002). This difference in the losses could be explained by the different distributions of basalt that occurred in the sample as a result of the difficulty of preventing some settlement during sample preparation

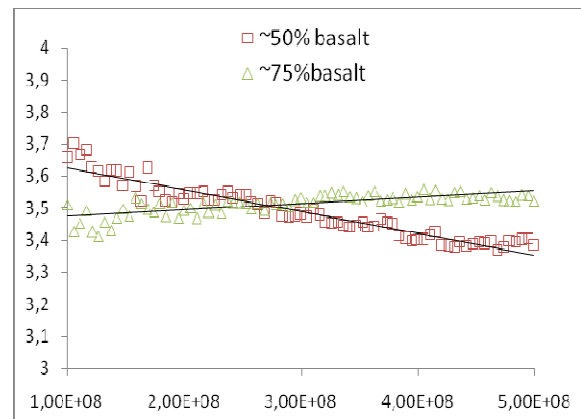


Figure 3: ϵ' as a function of ice contamination and frequency, for basalt and ice mixtures at -40°C.

Figure 3 shows the evolution of ϵ' , for basalt and ice mixtures, at -40°C, with two different ice contaminations, on the frequency range 100 to 500MHz. With ~50% basalt, ϵ' is between 3.7 and 3.4, and with ~75% basalt it's 3.5. On the figure, ϵ' is nearly equal for the 50% and the 75% contamination levels of basalt. This is due to the similar distributions of basalt powder that resulted from precipitation during sample preparation.

Concerning the evolution of the loss tangent for these two mixtures at -40°C , plotting curves on the frequency range 1-500MHz does not help in understanding the effect of ice contamination on dielectric properties because the losses are so weak ($\tan \delta < 0,06$) that we can not observe detectable differences between the two ice contaminations under the current setup.

In order to investigate the effect of the dust type contamination we measured four mixtures with different Martian-like surface dusts that have been used in the spectral calibration of TES instrument by the ARES group in JSC. The four samples have Mars-like amounts of iron oxides and are processed from the Hawaiian volcanic terrains (HMWK13: Plagioclase, Smectite, Eronite, Magnetite & Olivine; HWMK11: Plagioclase & Hematite; HWHP301: Plagioclase, Magnetite & Olivine; HWSP501: Plagioclase, Olivine, Magnetite & Hematite).

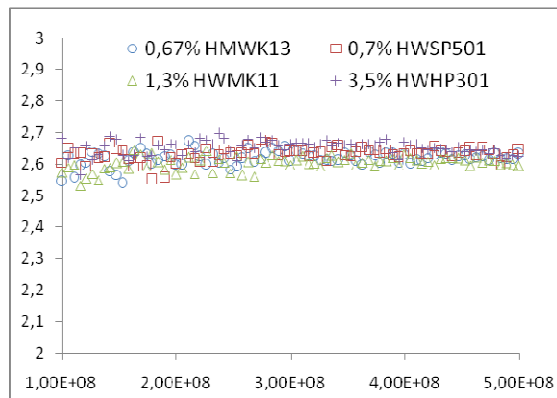


Figure 4: ϵ' as a function of dust type and frequency, for dust and ice mixtures at -50°C .

Figure 4 shows the evolution of ϵ' for four dirty-ices with very low concentrations of powder, made with varying types of dust, on the frequency range 100-500MHz at -50°C . We preferred to study low-concentration mixtures because it is more relevant to the polar deposits' first layers and because the mixture will be more homogeneous. As the dust concentration in our samples is very low (1 to 3.5%) the effect of dust type is not measurable. Our preliminary results suggest that with this low dust concentration ($<5\%$), whatever the dust type in the ice is, the real part of the permittivity is between 2.55 and 2.65 for frequencies fewer than 500MHz.

Concerning the evolution of loss tangent for these four mixtures at -50°C , as with the different concentrations of basalt in ice, plotting curves on this narrow range does not visualize the effect of dust type on dirty-ices'

dielectric properties, but have helped in constraining the ambiguities on the losses of the PLD-like material (i.e. $\tan \delta \sim 0,02$).

Discussion: These measurements show how different parameters can affect the dielectric behavior of dust and ice mixtures. The temperature has a strong effect on both real and imaginary parts of the permittivity because the proportion of unfrozen water is strongly related to this. The dust concentration in the ice is also important, but this parameter does not affect the permittivity linearly with the dust concentrations. It is better observed at moderate concentrations ($\sim 25\%$ dust) than for the high ones (e.g. $>50\%$ dust). The dust type in the ice should change the dielectric properties, but since we only studied very low concentrations of dust, we did not observe this parameter's influence. Finally, the last parameter that affects the dielectric behavior of dirty-ice is the frequency. Even though ice mixtures are non-dispersive materials, the observed frequency dependence was very weak on our measurement's range.

The laboratory measurements of ice-dust mixtures are very delicate and require a very strong accuracy assessment. Dielectric properties of dirty-ices are strongly dependant on mixture thermal stability and homogeneity. All the above discussed measurements suggest that the current setup and measurement algorithm developed in this internship can produce highly reproducible results for dirty-ices.

Implications: Our results highlight the dielectric complexity of ice-dust mixtures and their evolution as a function of the Mars geophysical and environmental parametric spaces. The knowledge gained from a better understanding of PLD geoelectrical's context, as derived from laboratory measurements, help to constrain the ambiguities in the penetration depths and in the identification of layers for both MARSIS and SHARAD [5]. Finally, the comparison of these lab measurements and the dielectric properties deduced from the MARSIS data will be useful to perform a more quantitative analysis of the Martian PLD physical properties .

References: [1] Heggy E et al. (2001) Icarus 154. [2] Paillou P et al. (2001) Geo.RL 28. [3] Bertheliet et al. (2005) LPSC 36. [4] Bandfield J.L et al. (2002) JGRE 107. [5] E. Heggy (2002), PHD thesis, University of Paris.

Phase Stability Effects and Partitioning of Nickel Using the Humphrey Composition

Colin Jackson¹, Justin Filiberto², Allan Treiman², Loan Le³; ¹UCSC, Earth & Marine Sci., CA 95064; ²Lunar and Planetary Institute, 3600 Bay Area Blvd., Houston, Texas 77058, ³ESC Group, Jacobs Sverdrup, Houston, TX 77258

INTRODUCTION: The transition metals Fe, Mn, Co and Ni, as well as Mg, are fundamental to stabilizing high temperature phases in basalts. Ni is of particular interest because it is the most compatible (enriched in crystal) of the divalent cations in basaltic systems. Numerous investigations [1-6] have documented partitioning behavior (enrichment in crystal or melt phase) of these elements in an attempt to gain insight into early magmatic processes. From this body of work Jones' model [7] emerged, which was later revised by Beattie [8] to account for newly published data and fO_2 effects. This study was undertaken to document the effect NiO on phase stability and how Ni partitions in the initial stages of crystallization at high pressures and temperatures

Longhi and Walker [9] have recently utilized the revised D_{ol-liq}^{Ni} ($D_{ol-liq}^{Ni} = Ni \text{ cation } \% \text{ ol.} / Ni \text{ cation } \% \text{ liq.}$) model [8] to explain the seemingly inconsistent array of nickel concentrations found on the moon; although Ni is observed to act compatibly throughout natural magmatic systems, the more magnesium rich Mg-suite lunar rocks contain 250ppm less Ni than the more evolved (less Mg rich) low-Ti lunar mare basalts [9]. For a bottom-up crystallization sequence (3.0 GPa depth using a degassed upper mantle composition) of a lunar magma ocean, Longhi's MagFox/MagPox suite of programs predicts D_{ol-liq}^{Ni} values < 1 (Ni enriched in melt over olivine) while Mg remains compatible during the first 10 % of crystallization when incorporating Jones' D_{ol-liq}^{Ni} model. Decoupling Ni from Mg (incompatible vs. compatible) would have profound implications for interpreting planetary Ni abundances and constraining conditions of core formation.

Initial experimental D_{ol-liq}^{Ni} values have matched those predicted, but the crucial early decoupling of Mg and Ni partitioning has not yet been duplicated.

Jones' model was calibrated using almost entirely terrestrial data. However, initial lunar olivine would have crystallized in a non-typical terrestrial system (i.e. devolatilized and Fe-Ni poor). Additionally, there is a lack of ultra-high temperature, near incompatible D_{ol-liq}^{Ni} data to validate the extrapolation of Jones' model into lunar magma ocean conditions. We have tested Jones' model using a synthetic Martian basaltic composition in hopes of addressing the ability of the model to accurately predict near liquidus (first 10% of crystallization) D_{ol-liq}^{Ni} values in non-earth terrestrial systems.

The Martian basalt, Humphrey, was chosen for this study because it has been well studied in the absence of Ni [10, 11]. This work provides a baseline to gauge what effect Ni has on phase stabilization. Because Ni is not commonly analyzed for in natural systems, its effects on phase stability are poorly understood and commonly overlooked. With a more complete understanding of Ni, its effects can better be compensated for in absence of complete chemical analysis.

METHOD: Our experiments were conducted at the Johnson Space Center High Pressure Laboratory using a piston cylinder press. A synthetic composition based on the Humphrey Basalt [12] plus NiO was made from a mix of oxides. This mix was fired at 1400° C and 1 atm to ensure minimal concentrations of H₂O and CO₂. The run product was then ground and stored in a desiccator. Once loaded into graphite capsules our samples were stored for a minimum of 12 hours at 150° C. The experimental assembly consisted of BaCO₃ sleeves along with crushable MgO spacers.

This assembly constrains fO_2 to QFM -1 to IW -1 [10,13]. Temperature was measured using a W5Re/W25Re thermocouple. Experiments were run using the piston out procedure (pressurizing to 2 kbar over intended pressure and then brought down at temperature). To ensure crystal-melt equilibrium samples were held at super liquidus conditions for 30 minutes before lowering to crystallization T where the sample equilibrated over 60 minute period. Major element analysis of our samples was completed using a Cameca SX-100 electron microprobe at the Johnson Space Center using synthetic oxides. Additionally, samples were analyzed for water content using a FTIR spectrometer at the Johnson Space Center. FTIR analysis found 0.1 +/- .1 wt. % water, consistent with other work using the identical assemblies and similar compositions [10]. To ensure complete analysis of mineral assemblages and gauge mineral abundances, mass balance calculations were conducted using the least squares computations of IgPet software.

RESULTS: Test of Jones' Model: A series of experiments were run at temperatures ranging from 1300-1420° C and 8 to 14 kbar to obtain D_{ol-liq}^{Ni} values at near liquidus conditions. These data are reported in Figure 1 along with Jones' D_{ol-liq}^{Ni} linear regression line. Equilibrium was checked by referencing experimental $D_{ol-liq}^{Fe}/D_{ol-liq}^{Mg}$ ratios to Jones' [14] published regression line. Experimentally determined D_{ol-liq}^{Fe} values are on average higher than Jones's values for a given D_{ol-liq}^{Mg} but are within 1 std. deviation and are consistent with published Martian basaltic data [10, 15].

Although D_{ol-liq}^{Ni} determined here for the Humphrey composition is always $\gg 1$ (Ni is always strongly compatible with olivine), it does match predicted values by Jones' model. Additionally, as suggested by Jones [14], this correlation is independent of temperature and pressure.

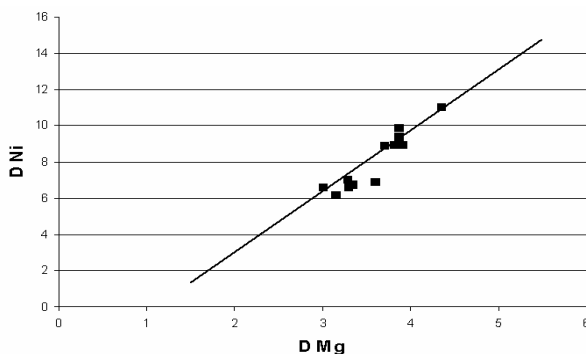


Figure 1: Humphrey $D_{ol-liq}^{Ni}/D_{ol-liq}^{Mg}$ plotted with Jones' 95 linear model (line)

Effect on Phase Relations of Nickel: Phase assemblages in the experimental products include glass, olivine + glass and olivine + pigeonite + glass. The high pressure pigeonite + glass stability field is poorly constrained due to the absence of data in the 16 kbar region.

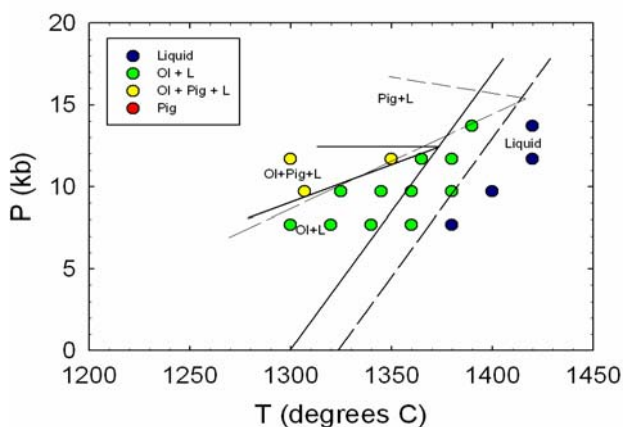


Figure 2: Phase Relations with Humphrey + Ni (dashed). Filiberto et al. Humphrey (solid line).

The implied multiple saturation point is shifted 3 kbar higher (15.5 kbar) when compared to nickel free system [10] as a result of the higher temperature liquidus and the unaltered slope of the pigeonite-in line.

DISCUSSION: Test of Jones' Model: The behavior of nickel in the Humphrey + NiO system supports Jones' model. Although D_{ol-liq}^{Ni} values gathered in this study do not address the validity of extrapolating to ultramafic systems, the independence of Jones' model from temperature and pressure effects

indicates extrapolation into initial lunar magma ocean pressures and temperatures may be valid. The success of Jones' model in predicting D_{ol-liq}^{Ni} values in a Martian system provides evidence that Jones' model can be applied to systems within other terrestrial bodies, such as the Moon.

The Fo component (molar Mg/(Mg+Fe)) of Humphrey + NiO is on average 5 points less when direct P/T comparisons are made with olivines produced in previous studies [10], indicating that Ni substitutes more-or-less for Mg in olivine. This competition could explain the decoupling of Mg and Ni that is required for Longhi and Walker's application of the Jones model to work.

Effect on Phase Relations of Nickel: The olivine saturated Humphrey + NiO liquidus is 25° C greater than that of Humphrey alone. The presence of Ni stabilizes olivine to higher temperatures than Mg and Fe alone due to its greater stability of Ni in olivine's crystal structure. This is evidenced by the higher average D_{ol-liq}^{Ni} value (8.30) compared to D_{ol-liq}^{Mg} (3.73), and by the greater heat of fusion of Ni olivine compared to Mg olivine (204 v. 113 kJ mol⁻¹) [8].

The addition of NiO did not, however, change the location of the pigeonite-in phase boundary [10]. This result is consistent with the near neutral partitioning of Ni and Mg into pigeonite ($D_{cpx-liq}^{Ni}/D_{cpx-liq}^{Mg}=1.4$). The unchanged pigeonite-in line leaves the higher pressure multiple saturation point (ol. + pig + melt) strictly as a function of the hotter liquidus. Further experiments at higher pressure will be needed to see how the pigeonite only liquidus curve is affected by NiO.

In summary, the addition of NiO to the Humphrey basalt forces olivine saturation to higher temperatures but pigeonite stability is basically unaffected.

ACKNOWLEDGEMENTS: I would like to thank Allan Treiman; truly the advisor of advisors. Secondly, I owe a debt of gratitude to my teachers, specifically Justin Filiberto and Jim Gill.

REFERENCES:

- [1] Hart H.R., Davis K.E., Nickel Partitioning Between Olivine and Silicate Melt, *Earth and Planetary Sci. Letters*, 40, 203-219, 1978 [2] Mysen BO, Partitioning of Samarium and Nickel Between Olivine, Orthopyroxene and liquid; Preliminary Data at 20 kbar and 1025°C, *Earth and Planetary Sci. Letters*, 31, 1-7, 1976 [3] Mysen BO, Nickel Partitioning between olivine and silicate melt: Henry's Law revisited, *American Mineralogist*, 64, 1107-1114, 1979 [4] Leeman W.P., Lindstrom D.J., Partitioning of Ni²⁺ Between Basaltic and Synthetic Melts and Olivines-An Experimental Study, *Geochim. Cosmochim. Acta*, 42, 801-816, 1978 [5] Nabelek P. I., Nickel Partitioning Between Olivine and Liquid in Natural Basalts: Henry's Law Behavior, *Earth and Planetary Sci. Letters*, 48, 293-302, 1980 [6] Takahashi E., Partitioning of Ni²⁺, Co²⁺, Fe²⁺, Mn²⁺ and Mg²⁺ between olivine and silicate melts: compositional dependence of partition coefficient, *Geochim. Cosmochim. Acta*, 42, 1829-1844, 1978 [7] Jones J.H., Temperature- and pressure-independent correlations of olivine/liquid partition coefficients and their application to trace element partitioning, *Contributions to Mineralogy and Petrology*, 88, 126-132, 1988 [8] Beattie et al, Partition coefficients for olivine-melt and orthopyroxene-melt systems, *Contributions to Mineralogy and Petrology*, 109, 212-224, 1991 [9] Longhi, Walker, Systematics of Ni and Co partitioning between olivine and peridotitic, Abstract, 2006 Fall Meeting [10] Filiberto et al., Crystallization Experiments on a Gusev Adirondack Basalt Composition, *Meteoritics & Planetary Science*, In submission [11] Monders et al, Phase equilibrium investigations of the Adirondack class basalts from the Gusev plains crater, Mars, *Meteoritics & Planetary Science*, 42, 131-148, 2007 [12] McSween et al., Characterization and petrologic interpretation and the olivine-rich basalts at Gusev Crater, Mars, *Journal of Geophysical Research*, 111, E02S10, 2006 [13] Holloway, J.R. et al., Melting experiments in the presence of graphite: Oxygen fugacity, ferric/ferrous ratio and dissolved CO₂. *European Jour. Mineral.*, 4, 105-114., 1992 [14] Jones J.H., Experimental Trace Element Partitioning, AGU Reference Shelf 3, 1995 [15] Musselwhite et al., Experimental petrology of the basaltic shergottite Yamato-980459: Implications of the thermal structure of the Martian mantle, *Meteoritics & Planetary Science*, 41, 1271-1290, 2006

GRAVITY MODELS OF LARGE IMPACT STRUCTURES ON ANCIENT MARS: IMPLICATIONS FOR IMPACT PROCESSES AND CRATER MODIFICATION

Michael S Kaplan¹, Walter S. Kiefer²; ¹Dept. of Earth Science, Rice University, 6100 Main St., Houston TX 77005, msk3782@rice.edu, ²Lunar and Planetary Institute, 3600 Bay Area Blvd., Houston TX 77058, kiefer@lpi.usra.edu.

Introduction: We analyze the gravity over large impact craters on Mars to constrain subsurface structure. The large craters and quasi-circular depressions (QCDs) are most likely from the Noachian and therefore their subsurface structure is indicative of impact processes on early Mars and subsequent crater modification. Our observations of the gravity over impact structures reveal positive gravity anomalies that resemble lunar mascons [1]. Modeling of some of these structures is impossible with surface loads alone and requires super-isostatic uplift of the mantle. In these structures, such as Newton, the uplift has remained for most of Martian history although the lithosphere was very thin at the time of impact [2]. Our results imply that QCD formation is not exclusively caused by viscous relaxation because this process would tend to eliminate super-isostatic uplift.

Methods: We use Mars gravity model MGS95J up to spherical harmonic degree 72, corresponding to a resolution of 300 km [3]. We therefore limit ourselves to examining craters with a diameter greater than 300 km to ensure that their gravity signatures are well determined. We use a high pass filter to remove the effects of anomalies with wavelengths too long to be correlated with the impact structure and use a cosine taper to reduce the effects of ringing. We remove the effects of both surface topography [4] and the compensating crustal roots using the elastic flexure model of Turcotte et al. [5]. These results as referred to as residual gravity. Because the large craters are typically quite old, we assume an elastic lithosphere thickness of 10 km, a typical value for Noachian crust [2]. Other parameters in the flexure calculation are also taken from McGovern et al. [2]. We assume a mean crustal thickness of 50 km [6]. Our results are only weakly sensitive to the assumed crustal densities of 2600 kg/m³ to 2900 kg/m³.

We examined the gravity signatures of both large visible craters [7] and of quasi-circular depressions [8,9], which are interpreted as

degraded impact structures [10]. Based on an initial survey of 21 impact structures with diameters between 290 km and 500 km, we selected six for more detailed modeling using the DISKGRAV model [11]. This model allows us to represent structures such as post-impact floor fill or uplifted mantle in terms of spherical caps of arbitrary size, thickness, and depth in the crust. The estimated thickness of post-impact floor fill is taken from the works of Howenstine and Kiefer [7] and Rosenberg et al. [9]. The densities of the modeled structures are varied depending on the petrology of the unit (e.g. impact ejecta, volcanic fill).

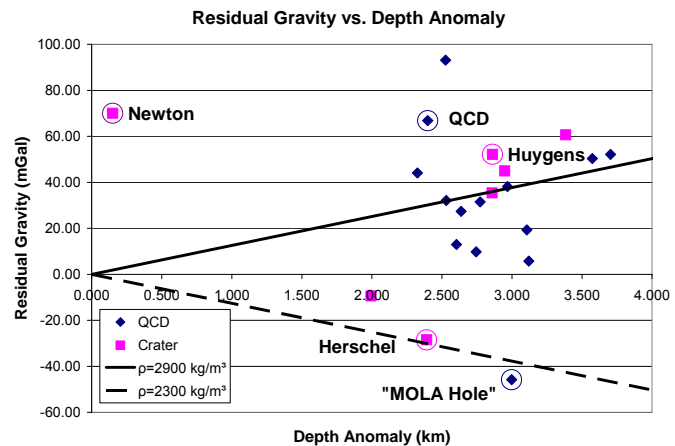


Figure 1: Scatter plot of residual gravity for 21 impact structures versus depth of post-impact floor fill. Circled structures are targets for detailed modeling. 18 of the 21 impact structures have positive gravity anomalies.

Results: Figure 1 shows the residual gravity anomaly as a function of post-impact floor fill, labeled depth anomaly. The solid and dashed lines define the range of gravity anomalies possible from post-impact floor fill alone. Structures that are above the solid line require the presence of some super-isostatic uplift of the mantle.

Newton, 326 km diameter, is a nearly pristine crater with less than 200 meters of post-impact floor fill [7]. This amount of fill is not

sufficient to explain the large positive gravity anomaly.

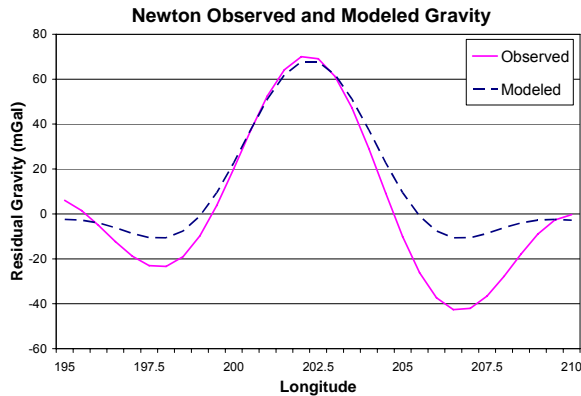


Figure 2: East-West residual gravity for Newton at -40.50 latitude. The solid line is the observed anomaly and the dashed is the modeled. The uplift is 9 km high with a diameter of 220 km.

Figure 2 shows the minimum uplift required to fit the data. The mantle is uplifted 9 km above the isostatic depth and is modeled with a diameter of 220 km. Equivalent fits are possible for decreased radii and increased uplifts until the mantle reaches the surface. Diameter of uplift and the height of uplift can not be independently constrained. However, the trade-off curve could be constrained in the future by the improved gravity field from Mars Reconnaissance Orbiter [12]. Our model fits the maxima of Newton but does not explain the negative gravity anomaly flanking the central peak. The small negative anomaly seen in our model is due to Fourier effects not large enough to match the observations. An annulus of low density material is outside of the crater rim, possibly due to ejecta. Future modeling this anomaly will improve our knowledge of the ejecta layer's thickness.

The QCD with a diameter of 418 km at latitude 30.45 and east longitude 48.52 has been informally referred to as the "MOLA Hole" because it was the first QCD identified with MOLA altimetry [13]. The gravity low is modeled with a surficial load of density 2250 kg/m³ and a diameter of 300 km, as seen in Figure 3. The load is representative of infilling due to ejecta with a possible contribution from a melt sheet. Probably due to the resolution of the gravity field, the peaks are off center by one degree.

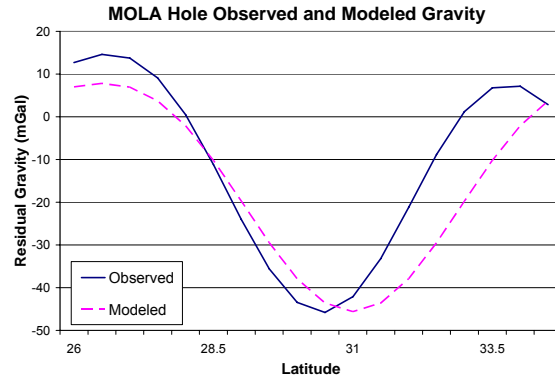


Figure 3: East-West residual gravity for the "MOLA Hole" at 48.52 longitude. The solid line is the observed anomaly and the dashed is the modeled. The model has a density of 2250 kg/m³, a diameter of 300 km, and depth of 3 km.

Similarly, Herschel (297 km diameter) can be modeled with 2350 kg/m³ fill, and possibly underwent a similar post-impact crater modification history. The results for the MOLA Hole and Herschel resemble those for the much larger Utopia basin, whose gravity signature may also be primarily due to post-impact basin fill [14].

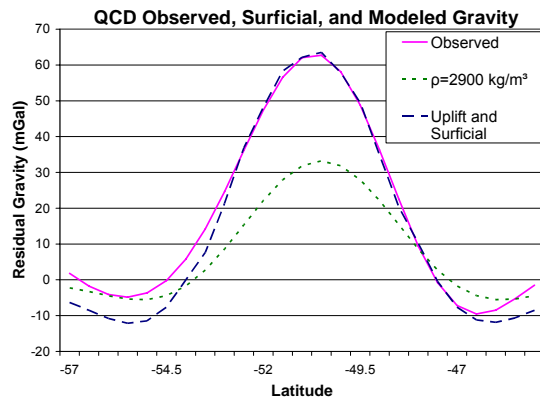


Figure 4: North-South residual gravity for the QCD at 294.1 longitude. The solid line is the observed anomaly, the short dashed line is the maximum surface load, and the long dashed is the combination of surface load and structural uplift. The surface load has a density of 2900 kg/m³, a diameter of 330 km, and a depth of 2.4 km. The structural uplift is 4 km with a diameter of 280 km.

Unlike the MOLA Hole, the QCD with a diameter of 330 km at latitude -50.55 and east longitude 294.1 can not be modeled with a realistic surficial load alone, as seen in Figure 4.

By modeling the maximum reasonable surface load and with the minimum amount of structural uplift to match the observed gravity, one can place a lower bound on the amount of structural uplift present. Using a surface load with the same diameter as the crater, a depth corresponding to the depth anomaly, and a density of 2900 kg/m^3 , a reasonable estimate for Martian basalts, the minimum mantle uplift required is 4 km with a diameter of 280 km.

Models of Huygens (474 km diameter) reveal a similar result. With the depth anomaly completely filled with basalt, there still must be at least 5 km of structural uplift.

Conclusions: The gravity results demonstrate that these impact structures have experienced a range of histories. The negative gravity anomalies at Herschel and the MOLA Hole suggest post-impact fill by low density material, such as impact ejecta. The small positive gravity anomalies at other structures (below the solid line in Figure 1) require denser fill, such as basaltic lava flows. Finally, structures with large positive gravity anomalies require the existence of several kilometers of super-isostatic uplift of the mantle. Preservation of this uplift for nearly 4 billion years may set important constraints on the thermal evolution of the Martian lithosphere.

One proposed model for forming QCDs is viscous relaxation of the original crater topography [15]. Our results require that several large QCDs have significant super-isostatic mantle uplift (Figures 1 and 4). This uplift would be destroyed by viscous relaxation of the crust. Thus, at least for these QCDs, some other mechanism, such as filling by post-impact lava flows, must be responsible for the subdued crater topography.

Ongoing work will assess additional features that influence the gravity signal of these craters, including the compensation state of the floor fill and of the dimensions and density of an impact melt sheet.

- References:** [1] Wieczorek and Phillips, *Icarus* 139, 246-259, 1999.
 [2] McGovern et al., *J. Geophys. Res.* 107, doi:10.1029/2002JE001854, 2002.
 [3] Konopliv et al., *Icarus* 182, 23-50, 2006.
 [4] Smith et al., *J. Geophys. Res.* 106, 23689-23722, 2001.
 [5] Turcotte et al., *J. Geophys. Res.* 86, 3951-3959, 1981.
 [6] Neumann et al., *J. Geophys. Res.* 109, doi:10.1029/2004JE002262, 2004.
 [7] Howenstein and Kiefer, LPSC 36, abstract 1742, 2005.
 [8] Anderson et al., LPSC 37, abstract 2018, 2006.
 [9] Rosenberg et al., LPSC 38, abstract 1460, 2007.
 [10] Frey et al., *Geophys. Res. Lett.* 29, 1384, 2002.
 [11] Kiefer, *EPSL* 222, 349-361, 2004
 [12] Zuber et al., LPSC 38, abstract 1461, 2007
 [13] Frey et al., *Geophys. Res. Lett.* 26, 1657-1660, 1999.
 [14] Searls et al., *J. Geophys. Res.* 111, doi:10.1029/2005JE002666, 2006.
 [15] Mohit and Phillips, LPSC 37, abstract 1975, 2006.

Forensic Analysis of Lunar Dust

J. Anneliese Lawrence¹, John F. Lindsay², Sarah K. Noble³. ¹Marshall University, Huntington, WV 25701 Lawrence21@marshall.edu; ²Lunar and Planetary Institute, Houston, TX 77058; ³NASA-Johnson Space Center Houston, TX 77058

Introduction: There have been twelve men that have walked on the moon. Although they could not imagine creating a permanent habitat on the moon, these astronauts gleaned vast amounts of information during their short stays and facilitated the planning to create the best possible station on the moon- a lunar habitat. While there, the astronauts collected lunar regolith with which to study and perform experiments. Regolith, or soil, is the loose material that covers the lunar surface. It is formed through billions of years of impacts.

One of these challenges that must quickly be solved is what those on the moon will wear while exploring and studying. The spacesuits from the Apollo missions were not meant for long term use. They were designed simply for a short day trip on the moon. Many lunar grains attached themselves to these suits, and while the dirt sticking to the suit is not inherently dangerous, the main issue is that the debris sticking to the suits can get brought into the habitats. The dirt can abrade the fabric over time, destroying the only barrier between human skin and the nothingness of the lunar environment. The toxicological affects of contact with and inhalation of lunar dust are still being studied, but minimizing such contact is the safest way to ensure astronaut health.

In addition, parts of the woven Teflon outer fabric on the outside of the suit were easily peeled off. The spacesuit engineers also added a layer of fiberglass which found its way to the outside of the suit and was frequently attached to our tape. Fiberglass can pose serious health problems; according to idph.com [1], "Smaller fibers have the ability to reach the lower part of the lungs increasing the chance of adverse health effects." They can also cause various other problems including sore nose, rashes and other skin irritations. There have been many new inventions and innovations in material science since the seventies and we need a new generation of space suits.

The goal of this study is to analyze dust lifted from Jack Schmitt's EVA space suit from Apollo 17 for mineralogy and grain size distributions for the sampled particles. This information will guide the design of the next generation of spacesuits as a necessary quality of each suit is resistance to lunar particles. Dangers to the engineering of the suits and the health of the astronauts

arise once these particles are attached to the suits. As of now, it is uncertain precisely what health problems may present from these lunar materials, but research is ongoing to determine safe level of exposure. This study will help toxicologists better understand the types of particles that are likely to be brought into a habitat by the astronauts.

Methods: In order to efficiently test the mineralogy and size distributions of grains stuck to the spacesuits, unorthodox methods were introduced. First, 3M magic tape® was, after extensive testing, placed onto the EVA spacesuit and peeled off in strategic locations to ensure even sampling of the suit as shown in Figure 1.

Then the pieces of tape were placed on carbon dots and carbon coated to remove excess charges under the electron beam. The samples were analyzed with a JOEL

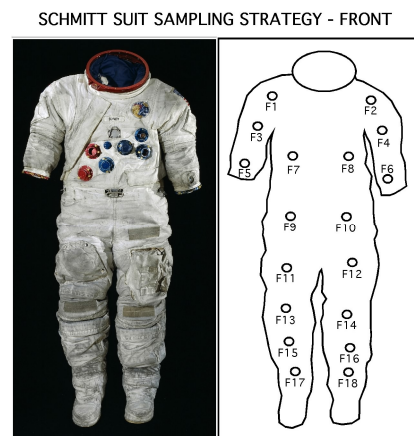


Figure 1. The sampling strategy for tape placement on the front of the suit. This process was also mirrored on the back of the suit.

5910 scanning electron microscope equipped with EDS at Johnson Space Center where we were able to view each grain in detail. Representative grains were photographed and EDS spectra taken to determine the chemistry and mineralogy of each particle (Fig.2).

The EDS, however, does have its limits. For grains below two microns, mineralogy could not be obtained, therefore all calculated grain sizes are limited by this constraint. From this chemical information and grain morphology, it was determined whether the grain was of lunar origin or terrestrial contamination. If it was lunar, the mineralogy was noted. Then, each photo was placed into ImageJ and each particle was separated and

measured. The exact areas were measured and diameters calculated, and then the size distributions were computed. Finally, by assuming spherical particles, the volume fractions of each mineral was calculated for the tape peel samples and was compared to that of typical Apollo 17 soils [2]. To arrive at the percent volume, it was assumed that all particles were spherical in shape and to ensure an accurate representative population, this process was repeated 1,200 times, of which 29.5% were contaminates, leaving 846 lunar particles, leading to a roughly 3.4% error. This does not take into account human error i.e. misreading the mineralogy or miscalculation of grain size which is possible considering the small size and high number of these grains.

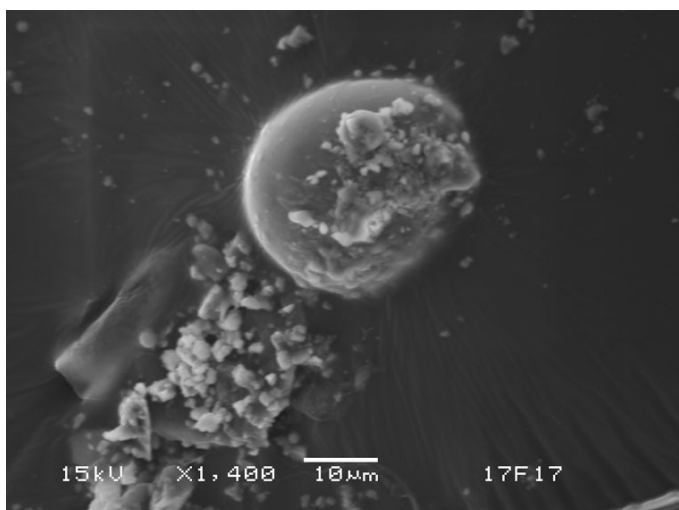


Figure 2. SEM secondary image of assorted grains from tape sample 17Front.

Results: Two things are calculated in the graphs below. The first three graphs are frequency graphs which show the most frequent grains found in each sampling area. To understand where each sample area starts and finishes take a look at Figure 1 once more. Sampling Area 1 encompasses region 1 through 4, Sampling Area 2 includes region 9-12 and Sampling Area 3 contains region 13-18. This includes both front and rear of the suit.

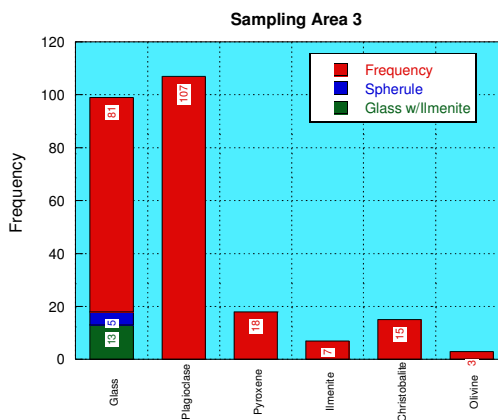
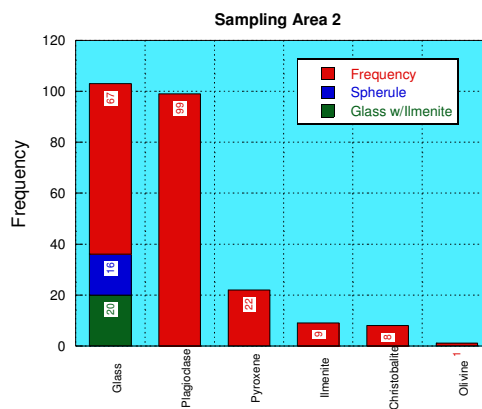
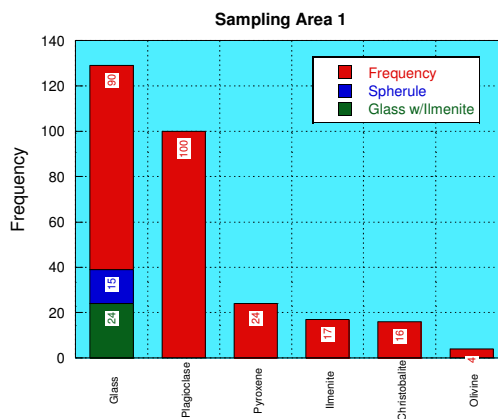


Figure 3. Frequency distributions of mineralogy for the 3 sampling regions detailed in the text.

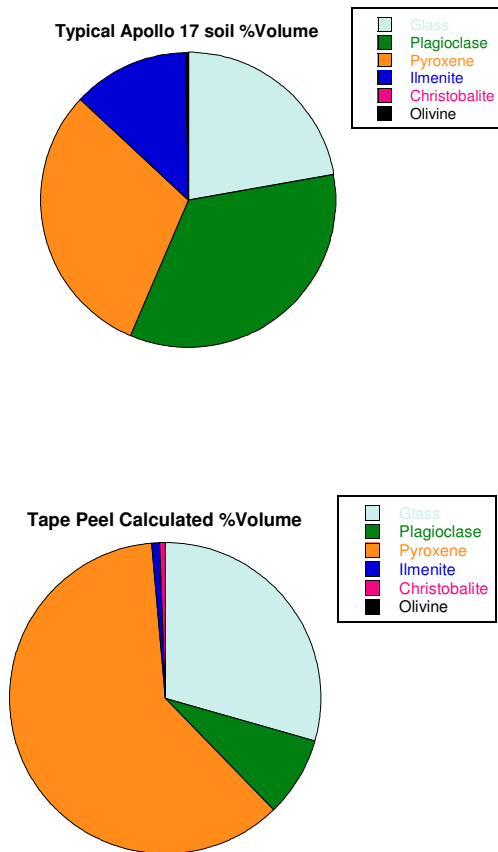


Figure 4. a) This chart is a breakdown by percent volume of lunar grain type for grain sizes between 20-90 microns from Apollo 17 (Mare soils 72501, 76501, and 78221) [2]. b) Percent volume graph for each lunar grain from the tape peels.

Agglutinates (lunar glass) and plagioclase were the most frequent grain found on the suit. There were almost 400 grains of lunar glass identified and nearly 350 grains of lunar plagioclase identified in this experiment alone. Many types of contamination including bits of Teflon, fiberglass, salt, calcium, and sulfur were also found on the tape peels. Furthermore, an average diameter for all grains was found to be 10.71598. The median was found to be 8.290083 while the mode was 5.498608.

Discussion: Some fascinating results were found in this research. As expected, most of the grains were ten microns or less, and as expected, most of the small grains were glass and plagioclase because they are easily broken down [3]. It was surprising to find that most of the volumes of grains attached to the suits were grains of

pyroxene. This was in contrast to the Ap17 soils. 58% by volume of the tape peel grains were pyroxene compared to only 30% in typical Apollo 17 soils [2].

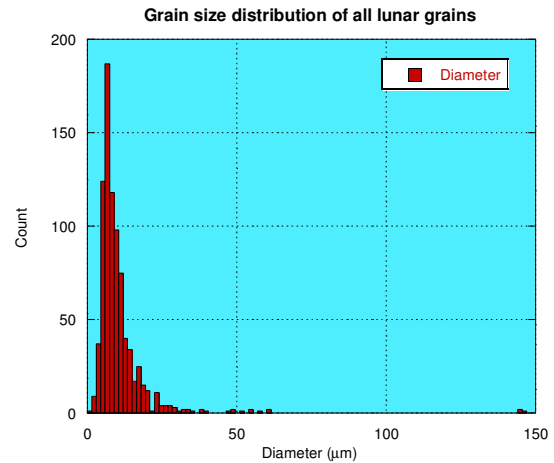


Figure 5. Grain size distribution for all grains of lunar origin.

Conclusion: The suits were covered with a layer of lunar dust even after being vacuumed and 30+ years of handling. This dust was more concentrated in areas such as the knees and elbows where significant wear on the fabric was also noted. Dust will be one of the major difficulties we must face on our next journey to the moon. Understanding its behavior in the lunar environment and its interaction with astronauts and their suits is important to ensure their safety. Some interesting results were found that suggest the composition of material clinging to the suits may differ from the typical soil composition of the area. Furthermore, it was found, as expected, that the clinging particles are generally small, which has implications for astronaut health and habitat design.

References: [1] Fiberglass Fact Sheet." Illinois Department of Public Health. 2 Aug. 2007 <<http://www.idph.state.il.us/envhealth/factsheets/fiberglass.htm>>. [2] Papike, J. J., and S. B. Simon. "Reviews of Geophysics and Space Physics." Diss. Institute for the Study of Mineral Deposits, South Dakota School of Mines and Technology, 1982. Abstract. The Lunar Regolith: Chemistry, Mineralogy, and Petrology 20 (1982): 795. [3] Horz F. and Cintala M. (1997) Impact experiments related to the evolution of planetary regoliths. Meteoritics and Planetary Science 32, 179-209.

Building a Hydrological Database for Martian Valley Networks

W. Pittman, Department of Computer Science and Engineering, University of Washington, Seattle, WA, 98195, USA (email: pittmanw@u.washington.edu)

Advisor: T.F. Stepinski, Lunar and Planetary Institute, 3600 Bay Area Boulevard, Houston, TX, 77058, USA (email: tom@lpi.usra.edu)

Introduction

Valley networks (hereafter referred to as VN) are landforms on Mars that are similar to terrestrial river systems [4,5]. Orbital imaging and global topographic mapping have demonstrated that VN dating to the Noachian are ubiquitous in the Martian highlands and also present in other parts of the planet. The current thinking is that most of the flows creating the valleys required precipitation, with the streamflow supplied either by runoff or precipitation-fed groundwater flow. Although the magnitude and persistence of flows carving these valleys remains uncertain, important clues as to the hydrologic environment prevailing on early Mars are recorded in the character of the preserved VN, and in particular, in their degree of integration.

In order to understand VN, investigators need to know where they are located. Mapping of VN is traditionally done manually through image interpretation. Carr [1] has compiled a global database of VN by interpreting Viking orbiter images. Currently this database represents the point of reference for subsequent, more detailed mapping of VN in small focus areas. However, Carr's database has a number of shortcomings. First, it is quite incomplete; the latest higher resolution images reveal many more valleys than are present in the database. Second, it is not coregistered with modern Martian spatial datasets; valleys on the map are not collocated with valleys on an image. Finally, because the valleys in Carr's dataset were drawn by hand, they are not topographically correct (even if they could be coregistered with topography). Overall, there is a need to construct a new, more complete, coregistered and topographically correct database of Martian VN.

Due to the required effort it is not feasible to construct such a database manually. Therefore, the focus has shifted toward automating the process of VN mapping. A VN mapping algorithm has been developed and tested [6], and applied to two quadrangles on Mars [3,9]. As expected, the application has revealed that the algorithm, in addition to identifying VN in details on par with precision manual mapping, also delineates channel-like features that are not VN. When applied to a large, but limited area, like a quadrangle, these false-positives can be identified by means of visual inspection. When constructing a global database,

however, a machine method of valleys validation has to be applied. Such method needs to be based on machine learning [11]. A machine learning technique uses a training set of expert-labeled VN to construct a decision (VN or no VN) function that is then applied to all candidate VN identified by the VN mapping algorithm. The result is a catalog of VN with a much reduced number of false-positives. A machine learning technique requires that each VN candidate is represented by a vector of attributes (numbers and categorical descriptors). The aim of this project was to calculate such attributes for VN candidates identified by the mapping algorithm.

Data

The data used in this project is the MOLA Mission Experiment Gridded Data Record (MEGDR) [8] that provides topography with the resolution of 1/128 degree. The mapping algorithm [6] uses this topographic data to calculate VN candidates over the entire surface of Mars. The result [Luo, private communication] is in the form of ArcGIS shapefile which can be overlaid on an image of the surface. This shapefile consists of 458,000 individual valley segments, each of which consists of a path described by (x,y) coordinates on Martian surface. The segments lack any numerical attributes, their purpose is to visually locate the fragments of VN candidates on a map. Another dataset used in this project is a global topography modified by a so called "flooding" algorithm. This algorithm fills all pits with a depth smaller than 100 m, which reduces the impact of post-valley formation cratering on topography. Finally, the global map of Martian geological units is also used.

Procedure

The database of VN is built using an ArcGIS script. This script, written in the Visual Basic for Applications (VBA) scripting language, has many steps and its full documentation is available upon request as an HTML document.

The purpose of the first step is to determine which segments are associated with each other and thus form a single VN candidate. The script scans through the valley segment data and looks for endpoints that share the same position. These associated segments are then collected together and assigned a valley network ID. The output of the first step is a shapefile

that is visually identical to the original input shapefile but contains only 184,000 objects – candidate VN. In the second step the script identifies a drainage basin (watershed) for each candidate VN. Each basin is further subdivided into constituent sub-basins in

order to determine the main stream for each network. Finally, in the third step, the script “reads” the values of raster variables, such as elevation and geological unit, underlying each VN candidate

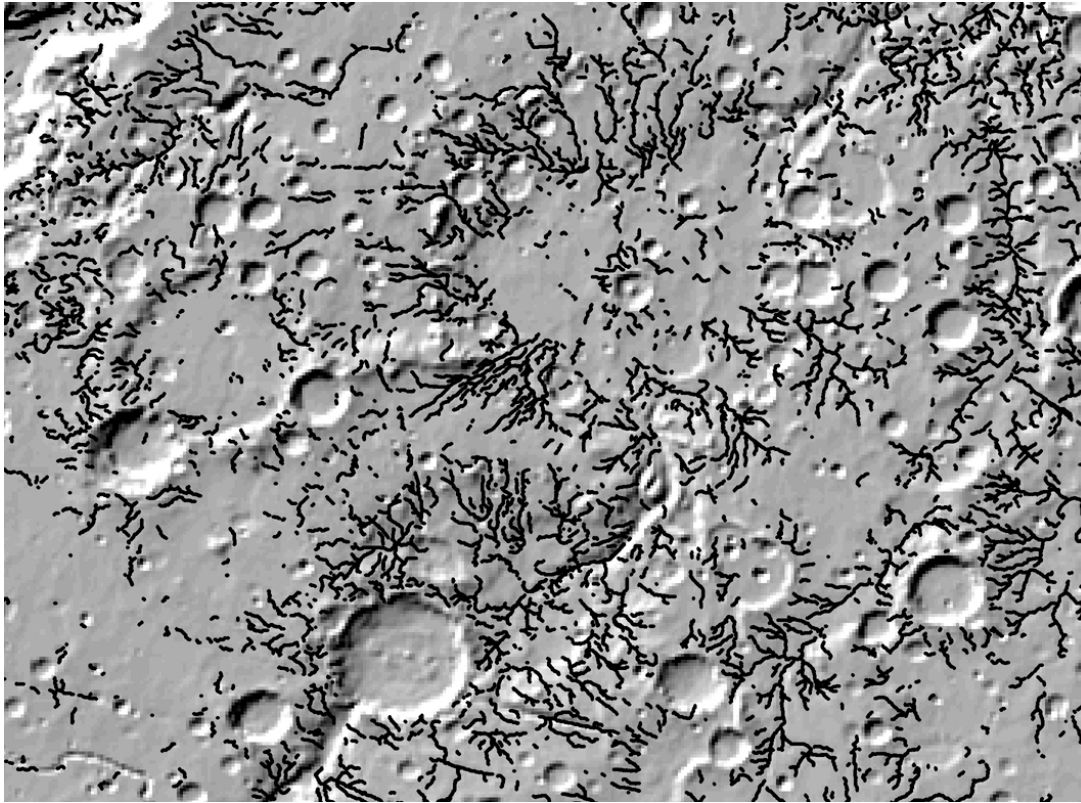


Figure 1. The site in the Margaritifer Sinus quadrangle on Mars. The underlying grayscale image shows topographic relief based on the MOLA measurements. The black lines indicate VN identified by the automatic mapping algorithm.

Results

The results of this project are three shapefiles: global map of VN candidates, global map of watershed boundaries, and global map of VN candidate outlets. The major result of the project is the attribute table associated with the map of VN candidates. This table contains numerical variables that would be used to distinguish between true VN and other channels. Also, for true VN, these values will help to understand their properties, and ultimately their origin.

Figure 1 shows a site located in the Margaritifer Sinus region. This site constitutes only a small fraction of the entire Martian surface, but it, nevertheless, contains a large number of VN candidates. The developed database cover this region and most of the rest of the Martian surface. It does not cover areas near the poles where VN are not present.

For each of the 184,000 VN candidates we list its ID number, coordinates of its outlet, its location (bounding box), a variable indicating whether the network has loops (about 2.3% of the VN candidates have loops and thus are non-dendritic; for such networks many attributes cannot be calculated), the underlying geological units, the number of segments in the network, network’s order and magnitude [2,7,10], as well as the total length of all streams in the network. Further, we list the length of the main stream, the elevation of the outlet and source of the main stream, its sinuosity, slope and aspect. Finally we give an area of drainage basin [2]. Figure 2 shows a few VN described by our database. Each network is shown in black. Its outlet is indicated by a gray dot, and its main stream is the longest stream from the outlet upstream. Associated drainage basin is shown in white.

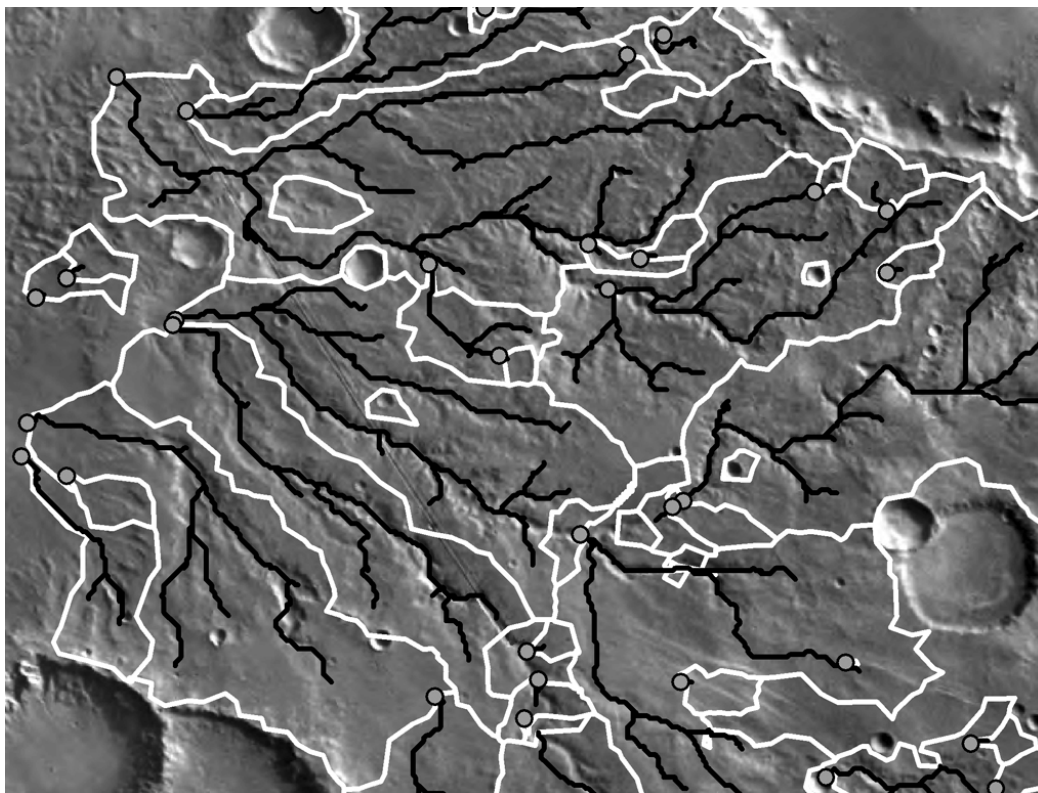


Figure 2. The Parana Valley site on Mars. The underlying Viking mosaic image shows VN. The black lines indicate VN identified by the automatic mapping algorithm, the white lines indicate boundaries of watersheds, and the gray dots indicate outlets.

Conclusion

A hydrological database of Martian VN has been constructed. This database provides a valuable tool for researchers studying the hydrology of early Mars. It could be used “as is” with a caveat that some “VN” may actually be different landforms. The attributes in the database will be used to apply a machine learning technique geared toward the automatic sorting of true VN from the other similarly looking landforms.

Acknowledgements

I would like to thank Dr. Stepinski for his guidance and ability to put up with my overoptimistic assessments of my progress, his collaborator Dr. Luo for saving us weeks by providing us with pre-modified data files, and Don Picos for providing me with \$3.50 enchilada Mondays.

References

- [1] Carr, M.C., 1995, The Martian Drainage system and the origin of valley networks and fretted channels, *Journal of Geophysical Research*, 100, E4, 7479-7507
- [2] Horton, R. E. 1932. Drainage-basin characteristics, *EOS Trans. AGU*, 13, 350-361.
- [3] Luo, W., Stepinski, T.F., “Topographically derived maps of valley networks and drainage density in the Mare

Tyrrenum quadrangle on Mars”, *Geophys. Res. Lett.*, vol.33, L18202, 2006.

- [4] Masursky, H., 1973, An overview of geologic results from Mariner 9, *Journal of Geophysical Research*, 78, 4009-4030
- [5] Milton, D.G., 1973, Water and processes of degradation in the Martian landscape, *Journal of Geophysical Research*, 78, 4037-4047
- [6] Molloy, I., and T.F. Stepinski. 2007. Automatic mapping of valley networks on Mars, *Computers and Geosciences*, 33, 728-738.
- [7] Shreve, R.L. 1966. Statistical law of stream numbers, *J. Geol.*, 74, 17-37.
- [8] Smith, D., G. Neumann, R. E. Arvidson, E. A. Guinness, and S. Slavney (2003), Mars Global Surveyor laser altimeter mission experiment gridded data record, MGS-M-MOLA-5-MEGDR-L3-V1.0, NASA Planet. Data Syst., St. Louis, Mo.
- [9] Stepinski, T.F., Luo, W., and Qi, Y., “Precision mapping of valley networks in Margaritifer Sinus, Mars”, 2007, XXXVIII LPSC, #1205.
- [10] Strahler, A. N. 1957. Quantitative analysis of watershed geomorphology, *EOS Trans. AGU*, 38, 912-920.
- [11] Witten, I.H., Frank, E., “Data Mining: Practical Machine Learning Tools and Techniques”, 2nd Edition, Morgan Kaufmann, San Francisco 2005.

AN ANALYSIS OF THE GEOLOGIC HISTORIES OF GANYMEDE'S DARK TERRAIN AND CALLISTO THROUGH IMPACT CRATERING DISTRIBUTIONS. E. G. Rivera-Valentin¹, M. R. Kirchoff² and P. Schenk², ¹Alfred University Dept. of Physics and Astronomy and Dept. of Mathematics (egr1@alfred.edu), ²Lunar and Planetary Institute (kirchoff@lpi.usra.edu, schenk@lpi.usra.edu)

Introduction: The analysis of impact cratering statistics allows for the inference of geologic histories and serves as a reliable tool to bring into light surface processes. It has been the major instrument in dating unsampled surfaces and effective in studying “the characteristics of asteroidal and cometary populations” [1]. In this project, we will use this technique to further compare and contrast the Jovian moons Ganymede and Callisto along with further analyzing Ganymede’s dark terrain.

It was found in an earlier project, which compared Ganymede’s relatively young light terrain to Callisto, that the impact population for the two bodies might be different [2]. By studying Ganymede’s heavily cratered dark terrain and Callisto’s surface, which has been found to be near saturation, we can better ascertain if a difference in the impact population does exist along with a further comparison of the two bodies.

With the new Galileo data, we can expand our understanding of the dark terrain, which covers one third of Ganymede’s surface. Since these regions include the oldest topography on Ganymede, we can further analyze Ganymede’s history by delving into its deep past granting us new insights into this satellite’s evolution. One of these being the ability to further evaluate Ganymede’s apex-antapex asymmetry.

Methods: Measurements of crater diameters were taken on mosaics created by Dr. Paul Schenk using the program qview. By taking two diameter measurements of a crater, an average diameter was recorded along with its coordinates. Crater diameters were recorded to at least 7 times the image resolution, but for plotting purposes only crater diameters at and 10 times above the image resolution were used. Palimpsests, which are “large, bright, circular, low-relief impact scars” [3], were included in the data sets by measuring the diameter of the continuous ejecta deposits, D_e , then finding the crater diameter, D_c , using the equation $D_c = \exp(\ln(D_e/2.442)/0.906)$ [4]. Checks were run on the counts to find any missed craters or double crater counts. Dr. Michelle Kirchoff, as yet another check on the crater counts, recounted one of the areas to verify that the counts were similar. To find the area in km^2 , the image was re-projected into an equal area projection then analyzed in ImageJ, which computes the number of pixels in the region and multiplies by the image resolution (km/pixel). All of this information was used to then create the cumulative and R plots. The cumulative plot is a log plot that graphs the crater

diameter versus the frequency by which that certain diameter appeared within the counted area. The R plot then bins the diameters and graphs them relative to a -3 cumulative slope on a log plot. This diagram allows for a more scrutinous analysis of the distribution function [1].

To analyze the counted areas on Ganymede for apex-antapex asymmetry along with other spatial crater density differences, the images were processed into ten degree thick slices relative to either the apex (0° , 90°) or the center of a proposed nearby basin. The counted area per slice was found in the same method as previously described. Using the distance equation for a sphere, the angular distance in degrees was found for every crater from its point of reference. This data was then plotted on a linear graph showing the angle from the apex or basin center (β) versus the crater density within a given ten-degree slice.

Results: Figure 1 shows the R plot of the global counts for Callisto along with all our counted regions. Our Callisto counts show approximately the same crater density and curve shape as the general Callisto curve. The Ganymede lines, with the exception of Galileo Regio, shows roughly the same shape as Callisto and is in the order of $\frac{3}{4}$ less densely cratered. Galileo Regio, on the other hand, is approximately one third less densely cratered than Callisto and about half as densely cratered than the other counted dark terrain regions on Ganymede. Its inflection point is also shifted more or less by 20 in crater diameter.

Figure 2 graphs the crater densities relative to the apex for the counted areas within Galileo Regio, Perrine Regio, and Marius Regio along with the general light terrain curve as reference. Most of the data, excluding Perrine Regio, shows on average an apex asymmetry by a factor of two, Marius Regio showing this more dramatically. Both Perrine and Marius Regio are shown to be at higher crater densities than the light terrain while Galileo Regio is seen to be at the crater density for light terrain.

In an investigative effort to answer why Galileo Regio seems to be distinctive from the other studied dark terrain, we plotted its crater densities relative to the distance from two proposed basins by Schenk *et al.* [5], which are 20.7°S , 179.2°W , “the least-square center of curvature for all furrows in Marius and Galileo Regio”, and 32°S , 189°W , “the best-fit center for all furrows in Galileo Regio”. This data is plotted in Figure 3 for crater diameters $D > 10$ and for diameters

$10 > D > 8$. The curve for the first basin shows an increase by a factor of 2 between the 35- and 45-degree bins and a general increase between the endpoints by a factor of 2 for craters $D > 10$. The data for diameters $10 > D > 8$ shows no such major fluctuations. The second basin shows an increase between the 55- and 65-degree bins and the 95- and 105-degree bins by a factor of 1.2 and a general increase between the endpoints by a factor of 1.5 for craters $D > 10$. Between the 95- and 105-degree bin for crater diameters $10 > D > 8$, an increase by a factor of 2.8 is found.

Discussion: Our Callisto data for the most part supports the global counts curve. The major difference is that “Callisto1” shows lower crater density for craters less than 5km. This can be due to regional statistics since we only provide one Callisto area whose resolution is that high.

In general, the dark terrains studied agree with most previous observations by being less densely cratered than Callisto [6]. This variance in crater density may suggest that Ganymede and Callisto have experienced differing amounts of tectonics, which could erode craters, or that the surface of Ganymede became rigid much later than Callisto’s surface impeding it from fully recording its impact history [7]. The dark terrain curves show approximately the same shape as the Callisto curves suggesting that the same impactor population most probably bombarded these two Jovian satellites.

Galileo Regio, in contrast, seems to have been resurfaced seeing that it was found to be half as densely cratered as the other investigated dark terrain. Since in the apex plot Galileo Regio appears in the crater density range for the light terrain, it is possible that this resurfacing event happened close to the creation of the light terrain, although most probably not under the same production scenario. We propose that an ejecta blanket mostly covers the counted area of Galileo Regio reducing its crater density. The basin plot provides clues to the existence of this crater. For the basin centered at 32°S , 189°W , the relative flatness of the graph between 55 and 95 may be taken to be the ejecta blanket coverage. The sharp increase in the crater diameter range of $10 > D > 8$ at the 105 bin may be considered to be the beginning of the secondary field. This region could have also had fluid flows from the interior creating smooth terrain as suggested by Casacchia *et al.* [7].

Our apex calculations show that an apex-antapex asymmetry exists by a factor of ~ 2 when observing Galileo Regio and Marius Regio. This value is less than what was found by Zahnle *et al.* [8], who found the asymmetry to exist by a factor of 4 on the light terrain, and is much less than the theorized value of 40. The lower factors in general may occur because the

surface of Ganymede rotated non-synchronously in the past [8]. The smaller differences for dark terrain with respect to the light terrain may hint to a geologic process that actively eliminates many but not all older craters like what is expected from a nearly saturated surface.

Conclusions: Our data shows that the same impact population bombarded both Callisto and Ganymede since the shapes of the R plot curves for both satellites are similar. The studied dark terrain is $\frac{3}{4}$ less densely cratered than Callisto suggesting that Ganymede’s surface became rigid later than Callisto’s and so does not show a full impact history. Galileo Regio, on the other hand, differs in shape from both our Callisto and other dark terrain curves and is found to be half as densely cratered as our studied dark terrain. Considering that the apex plot shows Galileo Regio having crater densities close to the same level as light terrain, we hypothesize that this region was recently resurfaced by impact ejecta from a large nearby basin making it relatively younger. We have also discovered that when considering the dark terrain only an apex-antapex asymmetry of a factor of ~ 2 is found. The apex-antapex curve for Perrine Regio, though, shows the opposite of what is expected. This requires further analysis of this region to attempt to explain this puzzling aspect. It would also be advantageous to have a wider data set for Nicholson Regio, which is in the same longitudinal area as Perrine Regio, so that we may analyze its apex-antapex plot to explore whether this increase really represents this longitude range. Also, having only counted two small Callisto areas has limited our analysis here, so exploring other regions would be required to fully develop a better understanding of the different geologic histories between it and Ganymede. Our basin plots for Galileo Regio do not definitively provide answers to the reason why it is different from the other dark terrain so an extended investigation of this area would also be valuable.

Acknowledgements: All mosaic images used in the crater counts were provided by Dr. Paul Schenk along with most of the spreadsheets used to analyze the data. Dr. Michelle Kirchoff provided the techniques used in this project along with much of the guidance. I would also personally like to thank both of my advisors and the LPI for this tremendous opportunity.

References: [1] Crater Analysis Techniques Working Group (1979) *Icarus*, 37, 467-474. [2] S. Seddio and P. Schenk (2006) *LPI Summer Intern Conference*, 22, 34-36. [3] K.B. Jones *et al.* (2003) *Icarus*, 164, 197-212. [4] P. Schenk and F. J. Ridolfi (2002) *Geophysical Research Letters*, 29, 1590. [5] P. Schenk and W. B. McKinnon (1987) *Icarus*, 72, 209-234. [6] Murchie *et al.* (1989) *Icarus*, 81, 271-297. [7] R. Casacchia and R. G. Strom (1984) *JGR*, 89, B419-B428. [8] Zahnle *et al.* (2003) *Icarus*, 163, 263-28

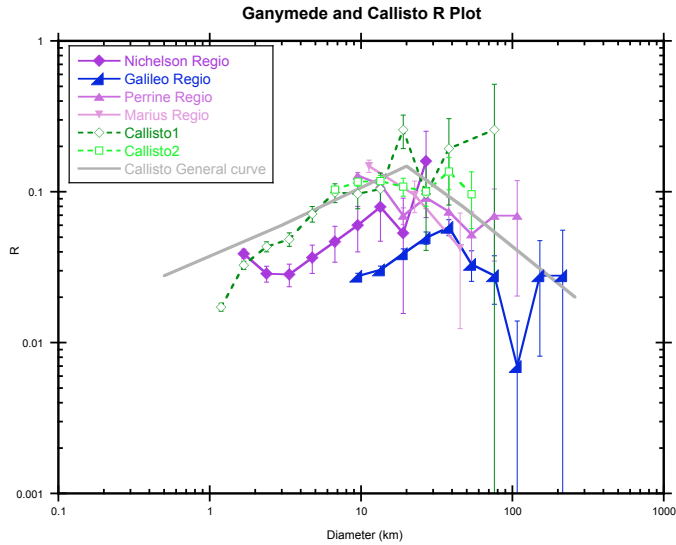


Figure 1: Complete R plot of all areas counted with the Callisto general curve for comparison. Callisto1 and Callisto2 are names chosen by the author for the two analyzed regions. The center coordinates for Callisto1 are 73°S, 90°W and for Callisto2 are 7.2°S, 6.6°W.

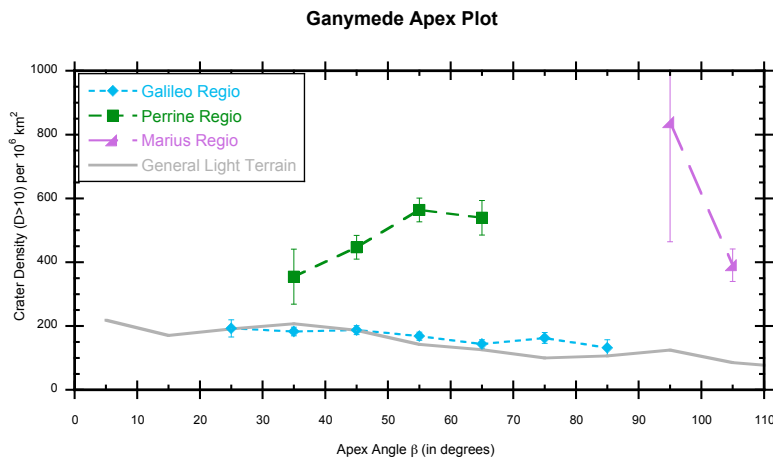


Figure 2: Apex plot showing the change in crater density with respect to the apex (0°, 90°) of Ganymede.

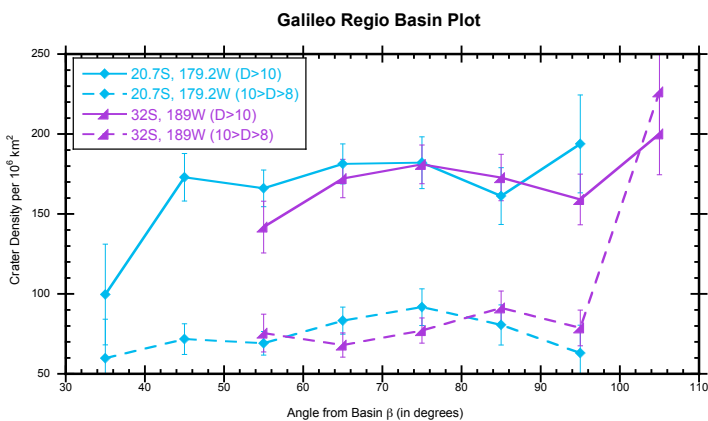


Figure 3: Basin plot showing the change in crater density with respect to two of the proposed basins nearest Galileo Regio.

THE GEOMORPHIC EVOLUTION OF SOUTHWEST ARABIA TERRA: SUPPORT FOR THE 2009 MARS SCIENCE LABORATORY LANDING SITE SELECTION PROCESS. M. R. Salvatore¹, C. C. Allen², D. Z. Oehler²; ¹Department of Geography, Penn State University, University Park, PA 16802. ²NASA – JSC, Houston, TX 77058.

Introduction: The Mars Science Laboratory (MSL) rover, which will launch in the fall of 2009, will assess whether Mars ever had an environment capable of supporting microbial life [1]. Seven proposed landing sites for MSL are located within southwestern Arabia Terra in our study region ranging from 10°N to 2°S and from 10°W to 8°E. This region encompasses an area of approximately 760,000 km², larger than the state of Texas, and lies immediately north of Meridiani Planum where the Mars Exploration Rover (MER) *Opportunity* has been exploring since 2004. In order to better understand the region’s history and to place the seven proposed MSL landing site candidates in a regional context, the geology and geomorphology of southwestern Arabia Terra have been analyzed and assessed based on a suite of remotely sensed data.

Methods: Lack of geographically-referenced Martian samples requires that geologic mapping and interpretation be performed using primarily orbital remote sensing. Thermal Emission Imaging System (THEMIS) nighttime infrared imagery was initially analyzed to map seventy-nine units within the study region. Mars Orbiter Laser Altimeter (MOLA) data were then incorporated, followed by THEMIS daytime infrared and THEMIS visible imagery, which were all evaluated together to reinterpret the region into five major map units. Fig. 1 shows the resultant geologic map of the study region.

Observations: The study region can be separated into five distinct units based on elevation, infrared emissions, and visible geomorphology. These five units include Uplands Material, Plains Material, Ridge-Forming Material, Scarp-Forming Material, and Flatlands Material. Their order of presentation below is from highest to lowest mean unit elevation.

Uplands Material: The most heavily cratered and variable terrain in the study region is comprised of Uplands Material (Fig. 2a). Numerous channels are visible in the southeastern region of this unit, only to become incorporated into the Ridge-Forming Material to the north. Arvidson et al. have interpreted this unit to be the oldest in southwest Arabia Terra [2].

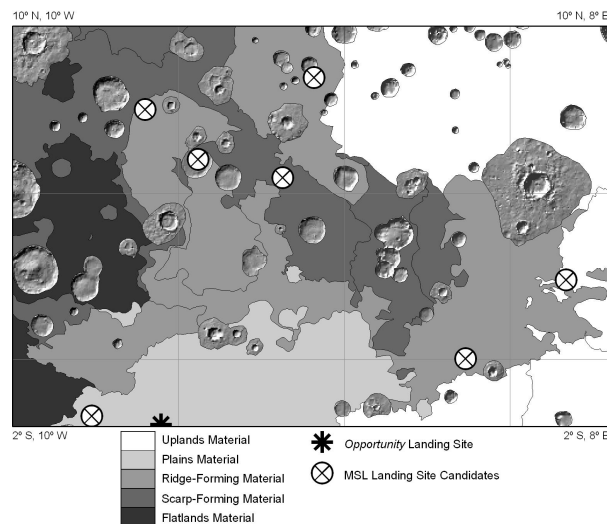


Fig. 1. Geologic map of southwest Arabia Terra. Large craters and ejecta were omitted for mapping purposes.

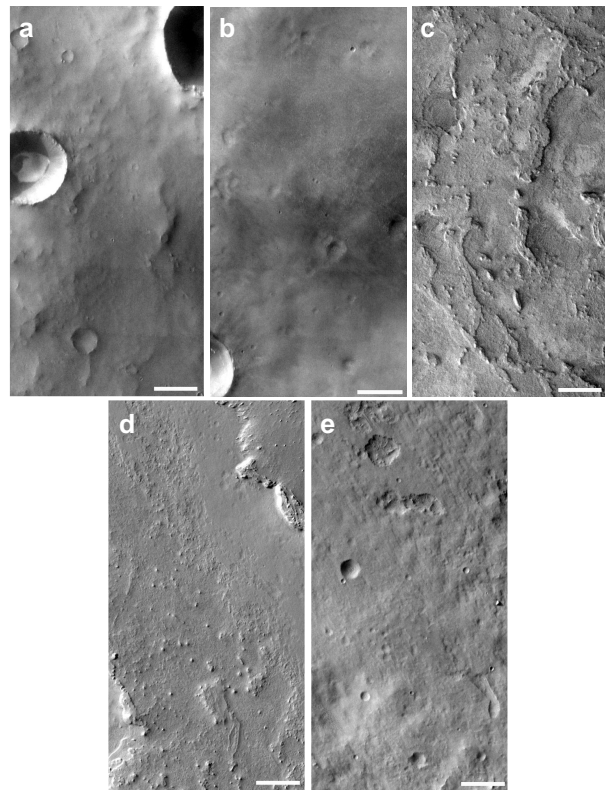


Fig. 2. Geologic/geomorphic units - THEMIS VIS imagery: (a) Uplands Material, (b) Plains Material, (c) Ridge-Forming Material, (d) Scarp-Forming Material, and (e) Flatlands Material. Scale bars = 2km. Subsets of THEMIS VIS images (a) V13169001, (b) V13082001, (c) V16176011, (d) V03720003, (e) V20307006.

Plains Material: The Plains Material is a smooth and lightly cratered unit. It has a varying brightness in THEMIS visible imagery, consistent with patches of aeolian dunes and exposed bedrock (which are smaller than the resolution of the THEMIS images) (Fig. 2b). It is associated with material found at MER *Opportunity*'s study region. This material appears to be only a few meters thick based on MOLA observations and data gathered from *Opportunity* [2]. This region also contains abundant crystalline hematite, as detected by the Thermal Emission Spectrometer (TES) aboard the Mars Global Surveyor (MGS) spacecraft [3]. The presence of this mineral, in addition to the sedimentary nature of the observed exposed bedrock, indicate that aqueous conditions were once present in this region of Mars [3,4].

Ridge-Forming Material: Just below the Plains Material is the distinct Ridge-Forming Material that dominates a large portion of this study region. This material is characterized by masses of arcuate to angular ridges with highly variable lengths and widths (up to more than 30 km long and more than 3 km wide), rising tens of meters above the surrounding landscape (Fig. 2c) [2,5]. These features show occasional braided relationships and appear to have a dominantly NNE/SSW orientation. Numerous hypotheses have been proposed for the formation of these ridges, including those involving volcanism [2] and the occurrence of diagenesis in the presence of groundwater [6].

Scarp-Forming Material: Located beneath the Ridge-Forming Material is a relatively flat unit containing numerous layers (Fig. 2d). Its dark appearance in THEMIS nighttime IR indicates a layer of dust over the entire region. As the name implies, steep scarps form at the unit's boundary with underlying units. Numerous small channels can be seen in the Scarp-Forming Unit in both Mars Orbiter Camera (MOC) and THEMIS visible imagery, supporting the argument that liquid water once played a role in the formation of this region (Fig. 3) [5].

Flatlands Material: The western portion of the study region is dominated by Flatlands Material, a moderately rough region below the Scarp-Forming Material. This region shows a range of brightness in both daytime and nighttime THEMIS infrared imagery, indicating variable dust coverage as well as local patches of exposed bedrock. The presence of large impact craters without visible ejecta suggests that this region is old and has been subjected to extensive erosion (Fig. 2e).

Interpretation: Based on regional geology and geomorphology, the southwest Arabia Terra study region appears to have experienced fluvial activity, followed by a more recent period of aeolian deposition and erosion. The presence of channels, minerals that

form primarily in aqueous conditions, as well as visible layering, both from orbit and ground (rover) observations, all support the theory that liquid water was present in this region. Mars Express's Observatoire pour la Minéralogie l'Eau, les Glaces et l'Activité (OMEGA) instrument has identified hydrated sulfates near 2°N, 0°E/W [7]. These minerals were undoubtedly formed in the presence of liquid water [8]. In addition, data obtained by *Opportunity*, including the identification of layered sediments, evidence of flowing water (festoon cross beds), and additional hydrated minerals, indicate that water most likely dominated at least the Plains Material in the past [4].

Over the past decade, MOLA data have exposed dozens of potential impact craters and basins that have previously been obscured and rendered indecipherable. One such possible impact basin is centered near 2°N, 1.5°W with an inner ring radius of approximately 190 km, an outer ring radius of approximately 350 km, and an annular trough located between the two rings (Fig. 4). Paleolake formation and other fluvial activity in conjunction with this impact basin and its related geomorphology may be associated with the hematite deposits seen in Meridiani Planum [10].

Some of the strongest evidence for fluvial activity includes the numerous channels that originate in the southern highlands and seem to disappear when they meet the Ridge-Forming Material to their north and northwest. It is possible that if a large impact basin (as speculated above) is responsible for the disappearance of these channels and if water existed on the planet's surface for long episodes, the Ridge-Forming Material may be the remains of a large megafan (M.J. Wilkinson, pers. comm., 2007). Common across much of the Earth, megafans are sedimentary features laid down by rivers over long periods of time. Megafans are defined as features (similar to alluvial fans) that are greater than 100 km in radius and typically have a slope of <1° [9]. The patterns of cross-cutting and bifurcation seen in the ridges of the Ridge-Forming Material are often seen in association with braided streams found in

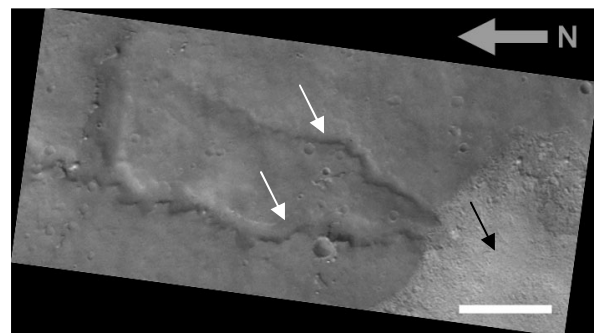


Fig. 3. A subsection of THEMIS VIS image V12457003 showing channels (white arrows) within the Scarp-Forming Unit emerging from underneath overlying Plains Material (black arrow). Scale bar = 2 km.

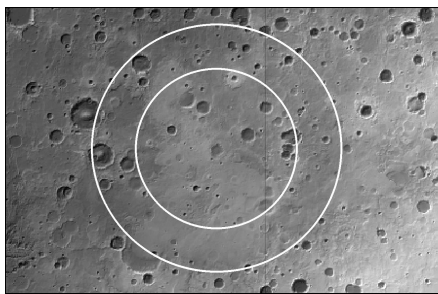


Fig. 4. A possible buried impact basin located in southwestern Arabia Terra. Shown are the theorized locations of the inner and outer rings.

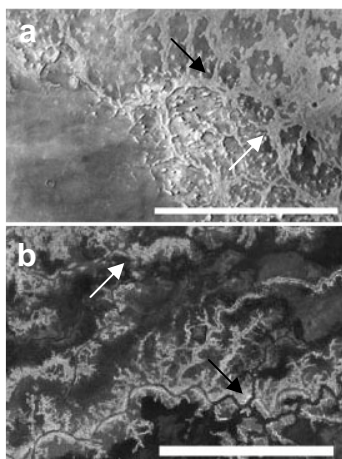


Fig. 5. (a) A subset of THEMIS VIS image V02284007 representing a subsection of the Ridge-Forming Material. (b) A LandSat visible image of channels within a terrestrial megafan located near 9.80° N, 26.70° E. Scale bars = 8 km. Cross-cutting (white arrows) and bifurcation (black arrows) are noted.

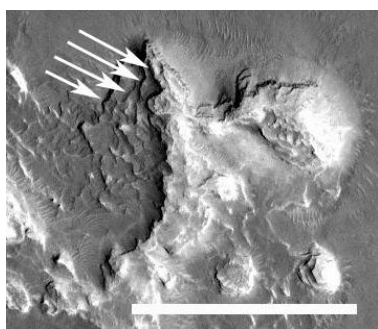


Fig. 6. A subsection of MOC image R1601540 showing visible layering within ridges of the Ridge-Forming Material. Scale bar = 1 km.

terrestrial megafans (Fig. 5). Preliminary studies show that the ridges of the Ridge-Forming Material are preferentially oriented in a NNW/SSE direction, which coincides with both the local and regional slope in which elevation decreases from the southeast to the northwest.

Layering is also evident within individual ridges of the Ridge-Forming Material (Fig. 6). This observation

is consistent with the deposits being sedimentary in nature [5].

Fig. 3 shows an example of channels in the Scarp-Forming Material that look as if they are emerging from beneath overlying Plains Material. One explanation is that channels of this nature were once widespread throughout southwest Arabia Terra only to be covered and obscured by overlying Plains Material.

Over a large portion of Mars' history, desert conditions have dominated the planet and wind has eroded much of the surface to produce the landscape we see today. Sand dunes and ripples throughout the study region, in addition to both large- and small-scale wind streaks and sand streaks, indicate that wind continues to play a role in sediment transport and surface morphology. Preferential erosion and preservation have occurred, likely due to past cementation and different rock compositions. The result is a highly variable surface that obscures clear evidence as to its formation.

Conclusions: In order for MSL to effectively search for past habitable areas, scientists must first understand what mesoscale characteristics are important to establish the necessary framework for life to exist. By mapping and interpreting the regional geology of southwestern Arabia Terra, context has been provided for seven potential MSL landing sites. Our work suggests that major fluvial processes have been important in southwestern Arabia Terra and thus could have enhanced habitability in this region. While aeolian processes have obscured much of the evidence of past liquid water, MSL is designed to find what evidence remains. If a landing site in southwest Arabia Terra is selected for this mission, MSL will undoubtedly uncover evidence of fluvial activity at some point in the Martian past.

Acknowledgements: I would like to thank Dr. M. Justin Wilkinson for his extremely helpful input and assistance in interpreting the region's geomorphology. I also thank the THEMIS Public Data Releases at <http://themis-data.asu.edu/> as well as the Malin Space Science Systems Mars Orbiter Camera Image Gallery at http://www.msss.com/moc_gallery/.

References: [1] A.R. Vasavada (2006) *MSL Landing Site Workshop*. [2] R.E. Arvidson et al. (2003) *JGR* 108(E12), 10.1029/2002JE001982. [3] P.R. Christensen et al. (2000) *JGR* 105(E4), 9623-9642. [4] S.W. Squyres et al. (2004) *Science* 306, 1709. [5] K.S. Edgett (2005) *Mars* 1, 5-58. [6] J. Ormö et al. (2004) *Icarus* 171, 295-316. [7] J.-P. Bibring et al. (2005) *Science* 307, 1576-1581. [8] J.L. Griffes et al. (2007) *JGR* 112(E08S09), 10.1029/2006JE002811. [9] M.J. Wilkinson et al. (2006) *J. S. Amer. Earth Sci.* 21, 151-172. [10] H.E. Newsom et al. (2003) *JGR* 108(E12), 10.1029/2002JE001993.

PHOTOCHEMICAL AND VERTICAL MIXING EFFECTS ON THE ATMOSPHERIC CHEMISTRY OF GLIESE 229B. Justin Troyer¹, Julie Moses², ¹Department of Physics, Purdue University, West Lafayette, IN 47906, ²Lunar and Planetary Institute, Houston, TX 77058.

Introduction: Gliese 229B is the first confirmed (Nakajima et al. 1995) and one of the best studied brown dwarfs. The observed infrared spectrum indicates that H₂O, CH₄, CO, and NH₃ are present in the atmosphere of Gliese 229B. However, the abundances predicted for several species by thermochemical equilibrium models (Fegley & Lodders 1996; Lodders & Fegley 2002), including CO, NH₃, and H₂S, are found to differ significantly from observed abundances (Noll et al. 1997; Saumon et al. 2000), with CO observed to be more abundant than predicted, NH₃ not increasing with altitude as predicted, and H₂S completely absent in the spectrum.

This model-data mismatch could possibly be explained by two main disequilibrium mechanisms: (1) vertical mixing that causes transport of gases to and from different atmospheric layers faster than the chemistry can equilibrate, and (2) photochemical reactions caused by the absorption of radiation from the parent star, Gliese 229A. Using the Caltech/JPL KINETICS code (Allen et al. 1981), a temperature-pressure profile of the atmosphere of Gliese 229B (Saumon et al. 2000), a composite spectrum of an M-type star, an extensive list of photochemical and thermochemical reactions, and basic data about Gliese 229B (mass, radius, separation from parent star, etc.), we have created a photochemical model of the atmosphere of Gliese 229B in order to determine whether disequilibrium effects like photochemistry and rapid mixing can explain the deviation of the abundances of CO and NH₃ away from thermochemical equilibrium.

Methods: We have developed a one-dimensional steady state model for the atmosphere of Gliese 229B that includes hydrogen, carbon, oxygen, and nitrogen photochemical and thermochemical reactions, vertical eddy diffusion, molecular diffusion, condensation, and radiative transfer (which includes Rayleigh scattering). We use the Caltech/JPL KINETICS code to solve the continuity equations for each molecular species in our model. The continuity equations are expressed as:

$$\frac{\partial n_i}{\partial t} + \frac{\partial \Phi_i}{\partial z} = P_i - L_i$$

where n_i = concentration of species, z = altitude, Φ_i = spatial flux of species i , P_i = production rate of species i , and L_i = loss rate of species i . The list of chemical reactions used is adapted from Sharp et al. (2004), with photolysis cross-sections taken from Moses et al. (2005). Calculations are made at 30° latitude, with the assumption of no obliquity. The vertical profile of the

atmosphere is split into 79 layers for calculations, with the bottom layer at a pressure of 300 bars and temperature of 2759 K, and the top layer at a pressure of 1.0×10^{-6} mbars and temperature of 268.1 K (see Saumon et al. 2000).

Input parameters for Gliese 229B are similar to those from “Model B” in Saumon et al. (2000), with $T_{\text{eff}} = 940$ K, $\text{Mass} \approx 36 M_J$ (Jupiter masses), an orbital distance of 44 AU, and a subsolar metallicity for Gliese 229B of $[\text{Fe}/\text{H}] = -0.3$. The eddy diffusion coefficient is a free parameter in our modeling. We look at three cases: $K_{zz} = 10^4$, $K_{zz} = 3 \times 10^5$, and $K_{zz} = 10^7 \text{ cm}^2 \text{ s}^{-1}$. The incident radiation file used is a composite spectrum of the M-type stars AU Microscopii (1150-1729 Å from the CoolCAT database¹), Gl 229A (1978-3200 Å from the MAST IUE Archive²), Gl 867A (1729-1978 Å, from the MAST IUE Archive), and Gl 411 (3200-8100 Å, from the STELIB, Le Borgne et al. 2003), since we were not able to find spectra for Gl 229A in the far UV and optical bandwidths. We also used the MAST FUSE archive⁴ to estimate the flux in the region from 900-1150 Å.

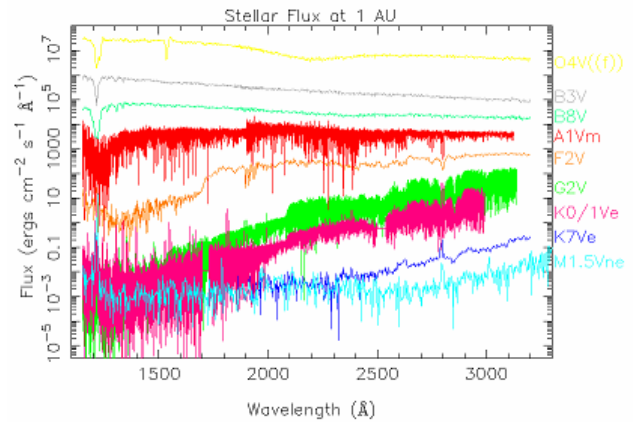


Figure 1. UV Spectrum for various spectral types, scaled to a distance of 1 AU. Spectral data for these plots come from MAST IUE, CoolCAT, and the IUE UV Atlas³, with distances found using Hipparcos parallaxes (ESA, 1997).

Results and Conclusions: Using data obtained from our model, we have found that the atmosphere of Gliese 229B is split into two regions, which is useful in trying to determine which effects are important in

¹ <http://casa.colorado.edu/~ayres/CoolCAT>

² <http://archive.stsci.edu/iue>

³ <http://www-int.stsci.edu/~jinger/iue.html>

⁴ <http://archive.stsci.edu/fuse>

the atmosphere. The lower section of the atmosphere is dominated by thermochemistry, due to the high temperatures and pressures found in this region, while the upper section of the atmosphere is dominated by photochemistry.

As molecules travel from the lower regions of the atmosphere up, they follow their equilibrium concentrations until they reach the point where the temperature is low enough that chemical timescales become longer than timescales due to diffusion. At this point, the parent species follow a constant mixing profile, with slight deviations caused by molecular diffusion and photochemical reactions, which go on to form different species with mixing profiles above those found at thermochemical equilibrium, as shown in Figure 2.

The main photochemical species produced by our model are CO_2 , HCN, and C_2H_6 . CO_2 production begins with the photolysis of H_2O , with the OH radical produced then reacting with CO to form CO_2 . HCN production begins when products from ammonia photolysis react with hydrocarbons to form C-N bonded species, eventually forming HCN. Production of C_2H_6 begins with either photolysis or thermochemical decomposition of CH_4 into CH_3 . Two CH_3 molecules then react with each other in the presence of a stable third atmospheric constituent to form C_2H_6 .

In order for CO_2 , HCN, and C_2H_6 to be observed by Spitzer, HST, or ground-based telescopes, their column abundances must be enhanced by several factors when compared to the column abundances found in the atmosphere at equilibrium, as found by Saumon et al. (2003). From our preliminary results, the column abundance of CO_2 is large enough that it should be observable, regardless of the eddy diffusion coefficient. HCN is also potentially observable, with larger eddy diffusion coefficients allowing easier discernability. C_2H_6 may or may not be observable, we cannot tell from information provided in Saumon et al. (2003).

The photochemistry in the atmosphere of Gliese 229B is relatively inefficient due to the fact that Gliese 229B has a large separation from its parent star. This is compounded by the fact that Gliese 229A is an M1/M2V type star. M-type stars have significantly less flux than solar type stars in near UV (see Figure 1), so photochemical reactions in the atmosphere of Gliese 229B would be less effective than if its parent star were of an earlier type. Thus photochemical processes are not the likely cause of the low observed NH_3 abundance or the higher than expected CO abundance. Instead, our data quantitatively confirm the suggestion of Griffith & Yelle (1999) and Saumon et al. (2000) that the observed disequilibrium abundances are caused by the fact that slow thermochemical kinetic

processes are unable to compete with more rapid vertical mixing as temperatures in the atmosphere decrease with altitude. The mixing ratios are “frozen in” when the mixing time scales drop below the chemical kinetic timescales.

Gliese 229A, like many other M-type stars is a flare star. These flares can have similar outputs to flares from the Sun, leading to a larger flux of charged particles being emitted by the star. The ions and other high energy particles released in these flares could initiate photochemistry in the atmosphere of Gliese 229B. However, we have not taken these effects into account in our model, and flare-induced chemistry could be an interesting avenue to explore with future modeling.

We plan to use similar methods as used with Gliese 229B to model the atmospheric thermochemistry and photochemistry for brown dwarfs found closer to their parent star and for brown dwarfs with an earlier type parent star, as these conditions would likely lead to greater photochemical production rates. We also plan future modeling for objects observed with Spitzer, to try and explain the observations.

Acknowledgements: I would like to thank my advisor, Julianne Moses, for all the time and effort she has put into this project, and for all of the helpful suggestions she has given me. I would also like to thank the LPI for giving me the opportunity to participate in this program, and all of the interns for making this summer an enjoyable and unforgettable experience.

Some of the data presented in this paper were obtained from the Multimission Archive at the Space Telescope Science Institute (MAST). STScI is operated by the Association of Universities for Research in Astronomy, Inc., under NASA contract NAS5-26555. Support for MAST for non-HST data is provided by the NASA Office of Space Science via grant NAG5-7584 and by other grants and contracts.

References:

- Allen, M. *et al.* 1981. *J. Geophys. Res.*, 86, 3617-3627. ESA. 1997. *The Hipparcos and Tycho Catalogues*, ESA SP-1200.
- Fegley, B. & Lodders, K. 1996. *ApJ* 472, L37-L39.
- Griffith, C.A. & Yelle, R.A. 1999. *ApJ* 519, L85-L88.
- Le Borgne, J.-F. *et al.* 2003. *A&A* 402, 433-442.
- Lodders, K. & Fegley, B. 2002. *Icarus* 155, 393-424.
- Moses, J. *et al.* 2005. *J. Geophys. Res.*, 110, E08001.
- Nakajima, T. *et al.* 1995. *Nature*, 378, 463-465.
- Noll, K., Geballe, T.R., & Marley, M. 1997. *ApJ* 489, L87-L90.
- Saumon, D. *et al.* 2000. *ApJ*, 541, 374-389.
- Saumon, D. *et al.* 2003. *ApJL*, submitted (astro-ph/0310805).
- Sharp, A.G. *et al.* 2004. *LPSC XXXV*. #1152.

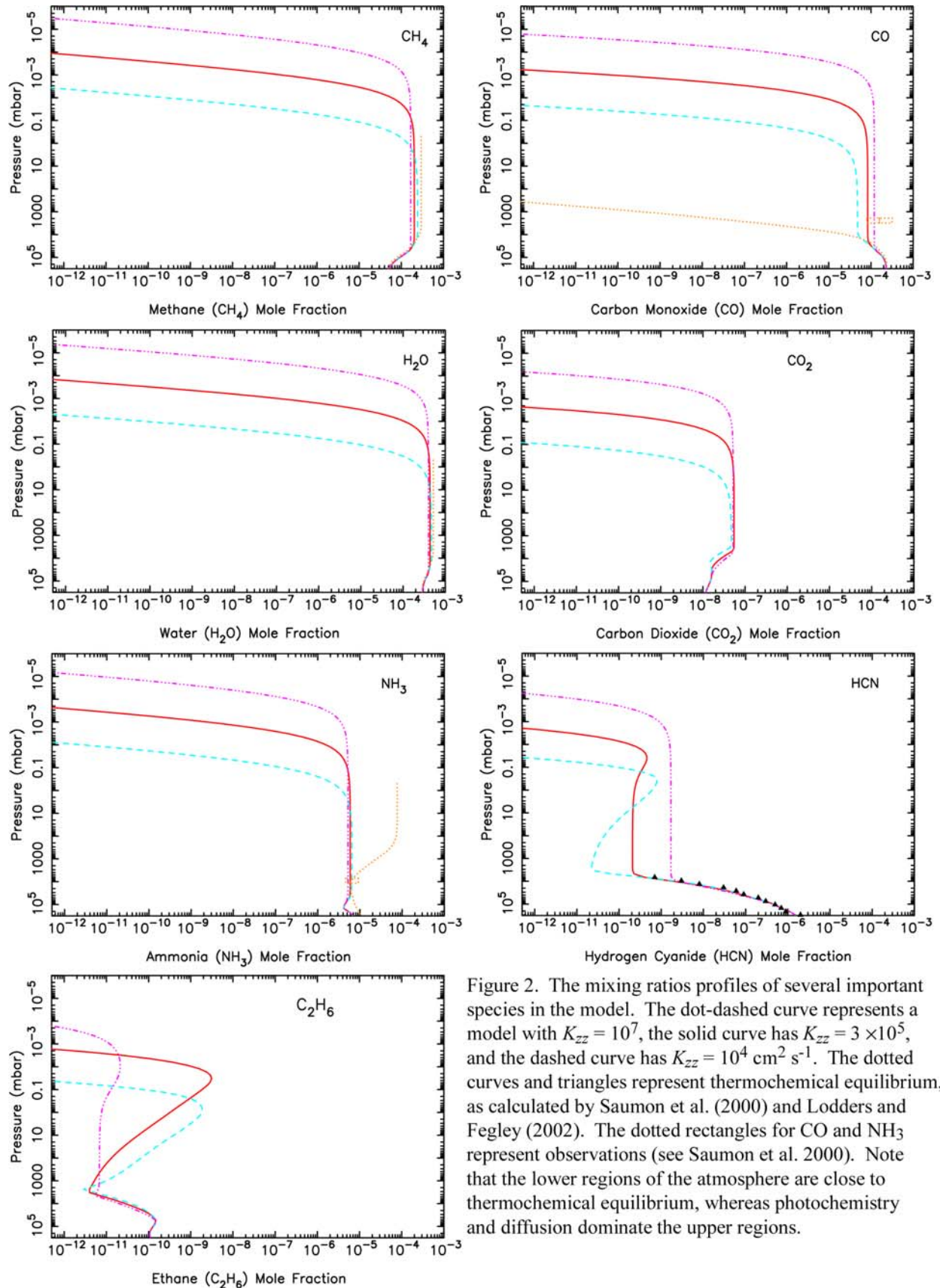


Figure 2. The mixing ratios profiles of several important species in the model. The dot-dashed curve represents a model with $K_{zz} = 10^7$, the solid curve has $K_{zz} = 3 \times 10^5$, and the dashed curve has $K_{zz} = 10^4 \text{ cm}^2 \text{ s}^{-1}$. The dotted curves and triangles represent thermochemical equilibrium, as calculated by Saumon et al. (2000) and Lodders and Fegley (2002). The dotted rectangles for CO and NH₃ represent observations (see Saumon et al. 2000). Note that the lower regions of the atmosphere are close to thermochemical equilibrium, whereas photochemistry and diffusion dominate the upper regions.

NOTES

NOTES

NOTES
